Application of Remote sensing and Spatial Data Integration Modeling to Predictive Mapping of Apatite-Mineralized zones in the Bikilal Layered Gabbro Complex, Western Ethiopia

Berhe Gebreselassie Abera

March, 2005

Application of Remote Sensing and Spatial Data Integration Modeling to Predictive Mapping of Apatite-Mineralized Zones in the Bikilal Layered Gabbro Complex, Western Ethiopia

by

Berhe Gebreselassie Abera

Thesis submitted to the International Institute for Geo-information Science and Earth Observation in partial fulfillment of the requirements for the degree of Master of Science in Geo-information Science and Earth Observation, Specialisation: Mineral Resource Exploration.

Thesis Assessment Board

1. Prof. Dr. F.D. van der Meer - Chairman (and first supervisor)
2. Prof. Dr. S.B. Kroonenberg - External examiner
3. Dr. E.J.M. Carranza - Second supervisor
4. Dr. P.M. van Dijk - Program director

INTERNATIONAL INSTITUTE FOR GEO-INFORMATION SCIENCE AND EARTH OBSERVATION
ENSCHEDE, THE NETHERLANDS

I will not use data used in the thesis that are owned by ITC or third parties for publishing without written permission of the ITC thesis supervisor.
I certify that although I may have conferred with others in preparing for this assignment, and drawn upon a range of sources cited in this work, the content of this thesis report is my original work.
Signed …….

Abstract

Applications of geological remote sensing and GIS-based spatial data integration for mineral potential mapping are still not fully integrated in the activities of Geological Survey of Ethiopia. The area of Bikilal Layered Gabbro Complex (BLGC) with associated apatite-magnetite-ilmenite deposits was chosen as a test area for the application of lithologic remote sensing and predictive mapping of potentially mineralized zones. The test area is remote and not easily accessible. It is also characterized by moderate to dense vegetation, presence of moderate to thick soil overburden, and scarce rock outcrops, which could render lithologic remote sensing difficult.

Landsat TM and ASTER data sets are available for testing and demonstrating usefulness of lithologic remote sensing. A systematic procedure, to select useful multi-spectral bands for lithologic classification, was followed and consists of the following. Spectral measurements from rock samples by PIMA (Portable Infrared Mineral Analyzer), descriptive statistical analysis of multi-spectral data based on published lithologic map, multi-spectral image transformations (principal component analysis and band ratioing) and multi-spectral image classification of lithologic units.

It was found that the Landsat TM data sets provide more useful information than the ASTER data set, in terms of lithologic remote sensing. The reason for this is that the Landsat TM data set was acquired during a relatively dry period, while the ASTER data set was acquired during the rainy season. Based on systematic analysis of multi-spectral image data, it was found that Landsat TM bands TM1, TM3, TM5 and TM7 and band ratios of TM7/TM2, TM5/TM2, TM5/TM1, TM5/TM4 and TM3/TM1 are potentially useful for lithologic remote sensing in the test area. However, using these potentially useful Landsat TM bands and band ratios in supervised image classification for lithologic mapping resulted in poor classification accuracy.

To improve discrimination of the different lithologic units of the test area, the Landsat TM bands were fused with digital elevation model (DEM) derived from the ASTER data set. The basis for image fusion is the noticeable differences in terrain features of the different lithologic units. A new lithologic map was created based on color composite images of fused potentially useful multi-spectral TM bands and DEM.

By SAM (Spectral Angle Mapper) classification of the Landsat TM bands, a mineral map was created. The mineral map indicates predominance of hornblende in the northern parts of the test area. This information supports interpretation of a different unit of meta-amphibole gabbro in the northern part of the test area is depicted in the new lithologic map. The mineral map also indicates presence of hydroxyl-apatite mineral in zones that coincide with known apatite-mineralized zones. This information also supports interpretation of prospective gabbro units depicted in the new lithologic map of the test area. The SAM-classified map and the new lithologic map suggest presence of undiscovered apatite-mineralized zones in the test area.

A predictive map of apatite-mineralized zones was created by using known apatite-mineralized zones as training variable and using the published lithologic map and the Landsat TM data as sources of explanatory variables representing recognition criteria for apatite deposits. The maps representing recognition criteria for apatite deposits include (a) proximity to olivine gabbro units, (b) proximity to faults/fractures digitized from published geological map and from derivative (filtered) images of Landsat TM data, and (c) TM5/TM4 band ratios reflecting clay-rich and iron-rich soil overburden in vicinity of known apatite deposits.

Predictive modeling of apatite-mineralized zones was carried out by application of evidential belief functions because (a) this method is appropriate to represent uncertainty in spatial data and (b) of perceivable presence of uncertainty (in terms of accuracy) of the data sets used to represent recognition criteria for apatite deposits. The resulting predictive map indicates that known apatite deposits coincide with predicted moderate to high potential zones. The results also show good to very good agreement between predicted moderate to high potential zones with the interpreted prospective gabbro in the new lithologic map and with the SAM-classified apatite pixels. Because of this, an optimized predictive map of promising exploration targets for apatite deposits was finally created by integrating predicted moderate to high potential zones, interpreted prospective gabbro and SAM-classified apatite pixels. The optimized predictive map of promising exploration targets for apatite deposits can be used, with caution, to guide further exploration of apatite deposits in the test area.

The result of the study indicates usefulness and limitations of application of remote sensing and spatial data integration modeling to map apatite-mineralized zones in the test area. Similar techniques can be applied to other areas with similar geologic settings.

Acknowledgements

I would like to forward my great thanks to the Geological Survey of Ethiopia and the Netherlands Fellowship Program for allowing and awarding me to pursue the scholarship in order to build-up my professional skill.

My special thanks and appreciation go to my first supervisor professor Dr. F. van der Meer, who is the chairman of the Department of Earth Systems Analysis, for his valuable advice, supervision, guidance, constructive suggestion, supports and help.

Great thanks and special appreciation go to my supervisor Dr. E.J.M. Carranza, who originally encouraged me to continue my study in geological remote sensing for the first time in area where I knew in my first-field excursion after university graduation and where I spent many years in phosphate exploration. I am grateful for his daily supervision, guidance, constructive suggestion and comments in all aspects in order to improve my understanding and reasoning. I appreciated those days I spent with him since those days are days of knowledge I gained.

I also extend my sincere gratitude to Drs. Boudewijn de Smith, who gave me a lot of basic knowledge in ITC starting from Module 1 and then in other specialization courses.

I forward my special thanks to Drs. Frank van Ruitenbeek, Dr. Tsehaie Woldai and Drs. Chris Hecker, for being available and standing ready to help whenever I need help and their warm welcome.

Finally I am grateful to thank all my best colleagues who contributed directly or indirectly in one or many aspects in improving the quality of this thesis.

Table of contents

List of figures

List of tables

Chapter 1: Introduction

1.1. General information

1.1.1. Mineral exploration activities of GSE

Mineral resources are important natural assets and it is a nation's best interests to stimulate a greater understanding of its indigenous wealth. Information on extent, quality and distribution of potential economic mineral resources is essential for an effective and informed decision, which is critical to meet the objectives of national socio-economic development.

To fulfill the above objectives, the Geological Survey of Ethiopia (GSE) was established in 1968 as a national institution responsible for geological mapping, ground geophysical surveys, mineral exploration and evaluation, as well as geotechnical, hydrogeological and geothermal activities. In addition to these, the survey collects, archives and disseminates earth science information to create earth-resources awareness among the population. Based on these backgrounds, GSE had conducted and continue to conduct several prospecting and exploration works to assess and locate indigenous phosphate and iron resources in different parts of the country mainly by using conventional field methods without the benefit of geological remote sensing methods.

1.1.2. Important mineral deposits of Ethiopia

The geological formations in Ethiopia range in age from Precambrian to Recent. The Phanerozoic sedimentary and volcanic rocks cover much part of the central highlands, rift valley and eastern lowlands part of Ethiopia. The Precambrian metamorphic rocks, which consist of low-grade volcano-sedimentary metamorphic rocks and high grade gneiss and schists, outcrop only in the northern, western and southern parts of the country. The most important economic minerals that are found in Ethiopia can be grouped into metallic minerals, industrial minerals and energy resources.

The **metallic** minerals, which are hosted mainly in the Basement rocks, include various occurrences of gold (Adola), platinum (Yubdo), rare earth elements, columbo-tantalite, copper, zinc, iron and nickel. Base-metal indications are also present in Mesozoic sediments.

The **industrial** minerals such as feldspar, marble, granite, talc, graphite, kyanite, mica, kaolin and quartz are mostly found in Precambrian rocks. The construction materials are hosted in Tertiary to Quaternary volcanics and sediments. Chemical raw materials of salt, sulphur and potash are mainly found in the Afar depression. Igneous phosphate, which is hosted in the Bikilal gabbroic rocks, is associated with iron-titanium minerals and it is the most promising potential for phosphate resources. The known reserves of apatite-magnetite-ilmenite deposits are 181Mt containing average of 3.5% P_2O_5 and 6 % TiO_2 (Consult 4 International, 2002) [11].

The **energy resources,** which include coal and oil shale, are also found within Cenozoic volcanics for example, the Yayu (SW of Ethiopia) have a thickness ranging from 4 to 25 m about 121 million tonnes of coal.

1.1.3. Importance of igneous phosphate (apatite) deposit

Some soil studies showed that most of Ethiopia's soils are deficient in phosphorus and nitrogen and need applications of chemical fertilizers to increase the fertility of the soils. The low fertility of the soil, which is a major agricultural production constraint, is a problem for the existing and future generations of this country whose economy is largely dependent on agriculture. Due to this, Ethiopia is forced to import processed fertilizer in order to increase the demand for phosphate fertilizer in the agriculture sector. The government of Ethiopia is doing not only to import but also to have a program for any opportunity to assess and to develop indigenous phosphate production. One of the efforts that have been made so far is to study the phosphate potential areas of Bikilal igneous phosphate deposit that has a promising raw material for phosphorus based fertilizer production in Ethiopia.

Adding fertilizers to soils and/or plants that are deficient in primary plant nutrients ((N-P-K) are vital to have a good plant growth, quality and quantity of crops. In sense of this, apatite is a mineral

that is very important raw material source for phosphate fertilizer production. Apatite can concentrate in different geochemical environments. In igneous complexes, apatite deposits are mainly confined to carbonatites, some nepheline-syenite complexes, alkaline ultramafic and basic intrusive complexes.

1.2. Research problem

The key elements in mineral exploration are to gain understanding of geologic area through lithological mapping and to assist in defining potential exploration targets prior to intensive field exploration activities. To map bedrock and identify presence and abundance of specific diagnostic minerals at specific scale, it is possible to use remote sensing methods. Remote sensing is an additional tool for geologist/researchers to understand the overall lithologic and structural history of the area and to define potential exploration targets, (Floyd F. Sabins, Jr., 1986) [32].

In Ethiopia, the lack of modern exploration methods, such as space-and airborne surveys combined with ground surveys, cause to take more time and money for studying large areas to delineate promising zones for more detailed studies by ground follow-up. The lack of a clear definition of geological features related with phosphate deposits and, consequently, the lack of a comprehensive phosphate potential map are among the major factors that contributed to the many years of studying limited areas for igneous phosphate exploration. There is also need to search for new deposits in less-known areas within the gabbroic intrusives occurring in the western Precambrian terrain. So far, all the previous studies have been done using traditional field exploration methods. GSE, however, has difficulty in accessing remotely sensed data, and remote sensing techniques have not been applied to explore for gabbroic-associated apatite mineralization.

The western Ethiopia Precambrian terrain constitutes several gabbroic complexes. The Bikilal layered gabbroic complex (BLGC) is one of the most interesting gabbroic complexes hosting igneous phosphate deposit. Unlike other prospective belts for phosphate deposit in the country, the Bikilal terrain is less explored. Thus, in the last 15 years, the Bikilal area has been the objective of several geological and mineral exploration studies. The aim was to produce a geological map at different scales by using available information and in most of the cases, the exploration efforts have been concentrated solely on known targets, whereas other zones have been practically left unexplored. Consequently, previous works on the integration of all available geological data to map phosphate potential of the terrain have been inadequate.

It is hypothesized that remote sensing can be useful in geological mapping and exploration for gabbroic associated apatite-magnetite-ilmenite bearing deposits. Many common rock-forming minerals can be detected by remote sensing because they have diagnostic spectral absorption features in the visible-near infrared (VNIR, 0.4 to 1.0 μm), short-wave infrared (SWIR, 1.0 to 2.5 μm), and thermal infrared (TIR, 8 to 12 μm) regions of the electromagnetic spectrum. These features are related to fundamental vibrational frequencies of anion groups such as SiO_4, PO_4, CO_3, and SO_4, and are diagnostic, exhibiting measurable variations such as band shifts with cation substitution that permit mineral species identification. For example, spectral-mineral groups, which can be mapped using Landsat TM and /or ASTER, SWIR data include carbonates, Al-OH, Fe, Mg-OH, H-O-H and Fe-oxide groups. In addition, analysis of five ASTER bands representing thermal emittance data permits estimation of silica content and, therefore, discrimination between siliceous, intermediate, and mafic rocks, (Hunt and Salisbury, 1970) [33], (1973) [34], Aussois (Modane), 1988) [4]. In view of this, predominant minerals of BLGC (e.g., olivine, clino-pyroxene (augite, diopside), ortho-pyroxene (enstatite, hypersthene), plagioclase, amphiboles (hornblende, actinolite), magnetite, ilmenite and apatite) are probably identifiable using ASTER and/or Landsat TM data. Therefore, from the economic importance of the gabbro-hosted apatite deposits in agriculture sector as raw material for making chemical fertilizer, it is envisaged to study usefulness of remote sensing techniques in detection of gabbroic rocks that could be prospective for apatite deposits.

1.3. Research objectives

The major objective of this study is to test usefulness of remote sensing in mapping of apatite-mineralized zones in the BLGC. To support this major objective, the research specifically aims to:

1. To determine which bands of Landsat TM and/or ASTER data are useful for lithologic discrimination in the Bikilal area.
2. To map the different lithologic units of the BLGC using Landsat TM and/or ASTER data.
3. To delineate unknown apatite-mineralized zones using Landsat TM and/or ASTER data.

1.4. Overall research methodology

The research will be carried out in four major phases. These are literature review phase, database creation phase, surface characterization phase and method development phase.

1. The literature review phase consists of previous exploration works of the area, previous works on lithologic remote sensing in similar geological settings and geological set-up of gabbroic rocks.
2. Database creation phase is undertaken to offer an organized mechanism for storing, managing and retrieving information using GIS operations.
3. The surface characterization phase consists:
    - PIMA analysis on representative rock samples - to know the general spectral properties of the major rocks and to select suitable bands (as suggestive information).
    - Spectral (or thermal) characterization - to determine spatial variability, especially in relation to lithology of DN-values in individual bands and/or band ratios of satellite images - to know the mean and mean ratio DN-value.

4. The method development phase is to study and test various techniques for geological remote sensing of various lithologic units based on the results of surface characterization phase. For example, band rationing, principal component analysis and image classification techniques (Maximum likelihood, etc). The last parts of this phase is devoted to spatial data integration modeling to delineate promising targets for further exploration of apatite deposits.

Chapter 2: Description of Study Area and Data Sets

2.1. Location and accessibility of Ghimbi-Bikilal area

The Ghimbi-Bikilal area (Figure 2.1) is situated in Oromia National Regional State, Western Wollega zone, Ghimbi Wereda, 441 km west of Addis Ababa. It lies between latitudes 9º3'20" - 9º21'06" N and longitudes 35º48'03"- 35º55'03" E. The area is accessible by a four-wheel drive vehicle through an asphalted road of 331 km from Addis Ababa to Nekemte and a fairly all weather road of 110 km from Nekemte to Ghimbi. The study area covers 412 km².

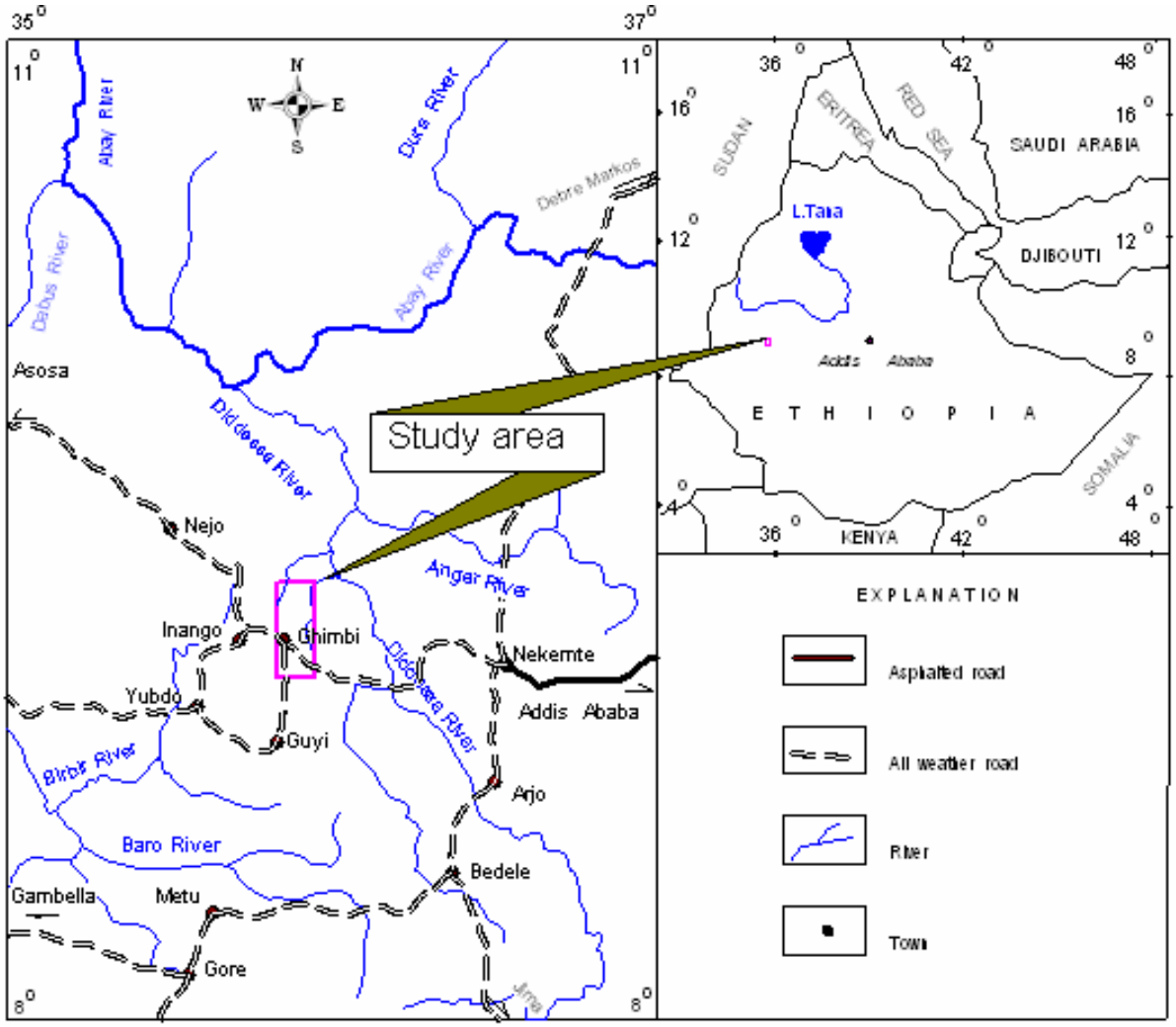

Figure 2.1: Location map of Ghimbi-Bikilal area (the whole area of the phosphate deposit)

2.2. Physiography

2.2.1. Landscape and topography

The Bikilal Mountain is mainly made up of a gabbro intrusive and has a maximum altitude of 2222 meters above mean sea level (a.m.s.l.). The phosphate deposit and surrounding area lie in a mountainous terrain at an altitude of 1400-2100 meters (a.m.s.l), with local relief as high as 500 meters. Slopes are commonly steep (15-40º), rarely gentle, and flat. The mountain slopes are overgrown by bushes, scattered trees and elephant grass.

Distributions of outcrops in the area are irregular and vary from place to place. Most frequently, outcrops occur along streambeds characterized by abrupt elevation changes and steep gradient, at minor divides and in the upper part of slopes. Blocks of substratum (floats) and elluvium usually 1-3

meters thick and occasionally reaching 11 meters cover the greater part of slopes including the ore zone in thickness. In gentle slopes, intense weathering is common such that saprolite is observed in pits and road cuts. There are several perennial small springs and streams draining the area. The major ones are Jejeba and Soti rivers that bounded the study area in the eastern and western side respectively.

2.2.2. Climate and vegetation

Climatic data can obtained from the Ghimbi weather station, which is located about 24 km south of the phosphate deposit. The mean maximum temperature is 26.5ºC (24.2ºC in July to 29.1ºC in March) and the mean annual rainfall is 1320.7 mm (2.0 mm in December to 396.0 mm in August). The driest seasons are in December to February, while the highest precipitations occur during June to September.

The Bikilal lies at the junction of two contrasting avifauna regions, the western Ethiopian low lands and the western highlands. The Bikilal area is situated between the Didessa lowlands to north and the highlands of Bikilal Mountain at 2222 meters. Due to this, within the area there are faunal mixes of lowland and highland species. The riverine forest and the tall elephant grass bush support a wide range of species at Bikilal.

2.2.3. Human activities and land-use

The Bikilal villages cover the area of known phosphate deposits located at the northern part of the study area and include Soji, Abo, Figa, Jire and Gerjo Villages. The inhabitants of the area are Oromo people, who lead their life by agriculture and breeding. The estimated population of the area as of 1995 is 3417. Most of the land of the area is cultivated and some of it is used for grazing. Land status of the area is suitable for cropping of coffee, maize, sorghum, teff and vegetables. The cropped area covers about 2964 hectares whereas the uncropped area is about 2287 hectares, (Western Wollega Administrative Zone Department of Agricultural Development, Landuse and Environmental Protection team at Ghimbi).

2.3. Previous geological works

2.3.1. Regional geological set up of Ghimbi-Bikilal area

Regionally, western Wollega is underlain by Precambrian rocks composed of gneiss, low-grade metamorphic rocks, which are further classified into metavolcano-sediments, marbles, mafic to felsic plutons, and minor ultramafics, which are intruded by syn- to post-tectonic granite and gabbro, later covered by Tertiary volcanics. The gabbroic plutons are mainly syn-tectonic and a few, including the Bikilal intrusive, are late to post-tectonic intrusive (Amenti A, 1989) [2].

Based on major differences in lithology, type of mineralization and field relationships, a tentative stratigraphic unit for Ghimbi-Bikilal area was erected from the oldest to the youngest as: biotite and/or granitic-gneiss, meta-amphibole gabbro, apatite-iron bearing meta-amphibole gabbro, olivine gabbro, granite, and granite and pegmatite dikes, (Efrem B., 2001) [18].

The **biotite and/or granitic-gneiss** occupy relatively high topography in the northern, north eastern, central east, southeastern, southern and southwestern part of mapped area (Figure 2.2). This unit is light gray to pinkish even dark gray in color. It varies from medium to coarse grained in texture and shows gneissose to granoblastic in structure. It consists mainly of quartz, K-feldspar, plagioclase and hornblende. Accessory minerals include muscovite, sphene, chlorite, zircon, epidote, garnet and ilmenite.

The **meta-amphibole gabbro** outcrops and runs a considerable distance from the village of Keki in south till the northern tip of the map area. It occupies high ridges and small hills in the northern, north western and central part of the target area. It is black to dark gray medium to coarse grained in fresh samples and shows reddish brown to yellowish color in weathered specimens. The major rock-forming minerals are plagioclase and green fibrous actinolite aggregates of hornblende after pyroxene,

showing relictic to granoblastic texture, with accessory minerals of ilmenite, apatite, chlorite, biotite, epidote, calcite, muscovite, sericite, rutile and sphene.

The **apatite-iron-bearing meta-amphibole gabbro** unit is found, stretching from the village of Keki to the northern part of the study area, as a series of small-disconnected alternating bands in a narrow belt zone within the meta-amphibole gabbro. Apatite-iron-bearing meta-amphibole gabbro is well pronounced in the NE part of the area shown as prospective gabbro in the geological map. It is dark green to greenish color, generally fine to medium grained. It shows well schistosity to granoblastic texture. It consists of hornblende, magnetite, muscovite, plagioclase, chlorite, and apatite with minor tremolite-actinolite, quartz and biotite. Apatite-iron-bearing meta-amphibole gabbro runs from a northeast-southwest strike direction and dipping towards northwest at 40-70º in the southern part of the unit and to a northwest-southeast, strike direction in the northern part of the unit with a south westerly dip angle ranging from 40^0-85^0.

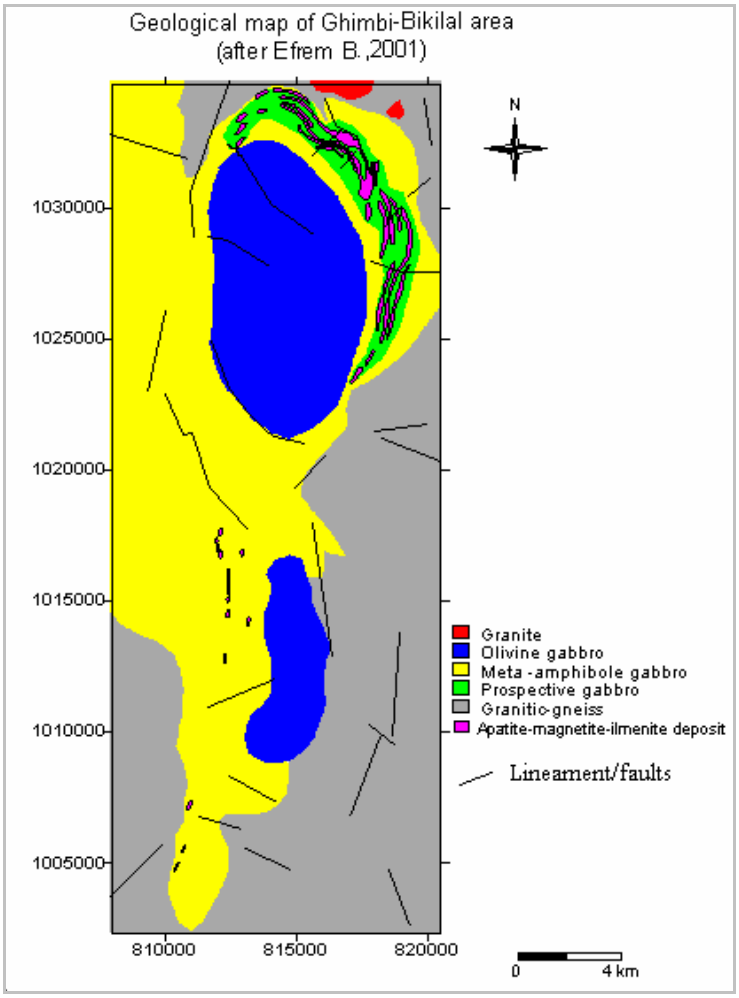

Figure 2.2: Geological map of Ghimbi-Bikilal area (After Efrem B., 2001)

The **olivine gabbro** occupies a ridge, which is east of Ghimbi town and in the central upper half portion of the mapped area. The olivine gabbro is dark color, medium to coarse grained composed mainly of plagioclase (labradorite), anhedral-subhedral pyroxene (augite), anhedral olivine, flaky biotite, and anhedral to subhedral opaque minerals. It is fresh, massive, and compact featured by local variation in grain size and composition from place to place; that is, it is medium-coarse grained and mafic-rich at the core with porphyritic crystals of pyroxene but is less-enriched in mafic minerals of pyroxenes and relatively fine grained towards the outer margin.

The **granite** unit, which occurs in the northern part of the area, consists of small unmappable mostly localized intrusions within the meta-amphibole gabbro unit. It is pinkish, white, light gray, fine to coarse-grained rock consisting of K-feldspars, quartz, plagioclase, and biotite. It shows granitic

texture under the microscope. Granite and/or aplitic dikes were observed in meta-amphibole gabbro, with an average thickness of 0.07-0.50 m and a length of 6-8 m. Besides, pegmatite dikes were also seen in biotite and/or granitic gneiss and meta-amphibole gabbro, with an average thickness ranging from few centimeters to half a meter and visible length of 10-15 meters.

Even though the Bikilal layered gabbroic intrusive as a whole extends from Bikilal as far as Ghimbi town for about 20 km south, the follow-up geological exploration works in the Soji-Gerjo Bikilal area were carried out mainly in the mineralized portion, which forms an elliptical zone around the olivine gabbro intrusive and measures about 12 km long and 9 km wide has been studied well. The mineralization zone is bounded by latitude 9º14'52"N and 9º21'48"N, and longitudes 35º51'42"E and 35º54'49"E. The mineralized zone has 0.7-1.2 km width in this part of the intrusive and there are scattered exposures of apatite-magnetite-ilmenite-bearing meta-amphibole gabbro throughout the extent of the intrusive. This area consists of meta-sedimentary rocks, basic rocks (olivine gabbro, meta-amphibole gabbro, anorthosite, diorite, ultrabasic rocks (apatite-magnetite-ilmenite-bearing meta-amphibole gabbro) and granitic-gneiss. The gabbroic intrusive itself is composed of zones (layers) of olivine gabbro at the core, leuco-gabbro (with minor anorthosite) and hornblende gabbro at the periphery which make up the bulk of the mass. A narrow zone of repetitive lenses-like thin and elongated horizons of meta-amphibole gabbro is intimately associated with massive and disseminated ilmenite and magnetite at places with apatite. This zone itself shows compositional and textural variation within it.

2.4. Mineral resources of Bikilal area

2.4.1. Iron ore deposits

The Bikilal Phosphate deposit is a complex Fe-Ti-P (phosphorus) mineralization of great regional significance. Detailed studies of the extent and volume of the various ores revealed that the tonnage of the iron ore deposit is 57.8 million tonnes (Mt) of indicted (C_1) and inferred (C_2), reserves, (EKIEP, 1988 phase II) [19]. The average grade of the total iron is 41.65% (23.29% magnetite iron), 0.36 % P_2O_5, 0.77 % S, 16.72%TiO_2 and 0.24%V_2O_5.

2.4.2. Apatite-magnetite-ilmenite deposits

The most common mineral deposits occurring in the area are apatite, magnetite-ilmenite and rare sulfides. The type of the apatite is hydroxylfluor-apatite variety (IFDC, 1987) [28]. The apatite-magnetite-ilmenite deposits are genetically intimately associated with the crystallization and intrusion history of the Bikilal layered gabbro intrusive. Fe-Ti-oxide-apatite association is common to gabbroic intrusive complex in the world. The ore deposit is syn-genetic segregated late magmatic type that is associated with a basic magma. As a result of this, the mineralized bodies are localized and restricted in a certain complex that is in basic petrographical zone. The mineralized rocks are composed of amphibole, chlorite, plagioclase, apatite, ilmenite and magnetite. From textural and mineralogical relationship point of view, beneficiation is possible by using grinding, magnetic separation and flotation methods.

The Fe-Ti-P mineralization occurs as lenses are hosted in the meta-amphibole gabbro. The nature of the contact between the mineralized lenses and the host rocks is not very clear. In some places, the contacts are gradational but in some places are abrupt. The preliminary resource of apatite- magnetite-ilmenite deposits of the Soji-Gerjo Bikilal, using results of outcrops, trenches and some core samples from boreholes of EKIEP was estimated 127 Mt to 200 meters depth, (Sisay A.,1992) [37], later revised as 141.09 Mt at reconnaissance stage, (Berhe G., 2001) [5]. The grade of this resource is in the range of 3-6 % P_2O_5. Further detailed studies were conducted at Soji-Bikilal area, which is part of Soji-Gerjo Bikilal that covers about 4.5 km² in order to delineate more apatite-bearing ore bodies and finally the mineable reserves were estimated 181 Mt at 3.5% P_2O_5 and 6.0% TiO_2 (Consult 4 International, 2002) [11]. The overall economic viability of this deposit has been conducted.

2.5. Available data sets

2.5.1. Multi-spectral digital datasets

Multi-spectral datasets of ASTER (Advanced Spaceborne Thermal Emission and Reflectance Radiometer) and Landsat TM (thematic mapper) are used in this study. The radiometric characteristics of ASTER and Landsat TM data are given in table 2 .1.

ASTER image data set:

The ASTER instrument was launched on the Terra satellite in December 1999 as part of the NASA Earth Observing System (EOS). It is one of five sensors on the Terra satellite and designed to acquire repetitive, high spatial resolution, multi-spectral data from the VNIR to the TIR region, the first time for any commercial satellite. It comprises three separate subsystems operating with three channels in the VNIR region (with 15 m pixel resolution), six channels in the SWIR region (with 30 m pixel resolution), and five channels in the TIR region (with 90 m pixel resolution).

Data granules AST_L1B.003:2006001688 and AST_L1B.003:2015319479 (path 170 and row 54), which were acquired in February 2002 are used in this study. These Level 1B products contain radiometrically calibrated and geometrically co-registered data for all ASTER channels. These products were created by applying the radiometric and geometric coefficients to the Level 1A data. The bands have been co-registered both between and within telescopes, and the data have been resampled to apply the geometric corrections. The Level 1B radiances are generated at 15 m, 30 m and 90 m resolutions corresponding to the VNIR, SWIR and TIR channels respectively, (http://ww.science.aster.ersadac.or.jp/en/about_aster/sensor/tokutyou.html), [26]. The swath width of the ASTER imagery is 60 x 60 km.

The Landsat TM data set:

The Landsat TM is a multi-spectral scanner with seven channels. Landsat TM imagery has been widely used for geological mapping applications. There are three basic classes of spectral information that can be obtained information from Landsat TM imagery for geological purpose in identifying the presence of iron bearing minerals/rocks in the visible (TM1, TM2 and TM3), hydroxyl or carbonate groups as well as hydrous minerals in rocks/soil in the mid infrared (TM5 and TM7) and the intensity of green biomass in the near infrared (TM4). The swath width of the Landsat TM is 185 x 185 Km, altitude 705 km and orbit type Sun-synchronous. A sub-scene of Landsat TM (path 170, row 54) acquired 8 March 1986 was used. It has 7 bands with (TM1 to TM5 and TM7), which have a 30 m and thermal TM6 of 60 m spatial resolutions.

Table 2-1: Radiometric characteristic of ASTER and Landsat TM bands

Region of Spectrum	Spatial Resolution	Spectral Range (µm)	ASTER Bands	Landsat Bands	Spectral Range (µm)	Spatial Resolution
VNIR	15 m			1	0.45-0.52	30 m
		0.52-0.60	1	2	0.52-0.60	
		0.63-0.69	2	3	0.63-0.69	
		0.76-0.86	3N (nadir looking)	4	0.76-0.90	
			3b (backward-look)	8	0.52-0.90	15 m
SWIR	30 m	1.60-1.70	4	5	1.55-1.75	30 m
		2.145-2.185	5	7	2.08-2.35	
		2.185-2.225	6			
		2.235-2.285	7			
		2.295-2.365	8			
		2.360-2.430	9			
TIR	90 m	8.125-8.475	10			
		8.475-8.825	11			
		8.925-9.275	12			
		10.25-10.95	13	6	10.40-12.50	60 m
		10.95-11.65	14			

2.5.2. Analogue data sets

Geological maps:

The geological map of Ghimbi-Bikilal area (1:50,000 scale), which has 412 km², covers the whole Bikilal layered gabbroic complex starting from 20 km south of Ghimbi town and extending up to 26 km north of Ghimbi town. The main rocks of the Ghimbi-Bikilal area are olivine gabbro, meta-amphibole gabbro, the apatite-magnetite-ilmenite mineralized meta-amphibole gabbro (Efrem B., 2001), [18] granite and granitic-gneiss. Detail geological map of Soji-Gerjo Bikilal area (1:10,000), with 46 km² that covers the most prospective for apatite and iron in the NE part of the geological map of Ghimbi-Bikilal area. It consists of several units of basic rocks (porphyritic and massive olivine gabbro), meta-amphibole gabbro, leuco-gabbro and/or anorthosite, iron-ore-bearing and apatite-bearing meta-amphibole gabbro, diorite, granitic dyke, meta-sedimentary rocks, migmatite and granitic-gneiss.

Topographic map:

The whole area is covered by the topographic map at 1:50,000 scale, which was published by the Ethiopian Mapping Agent in 1983. The topographic map consists of the Sayi and Ghimbi sheets covering the northern and southern part of the study area respectively were used for georeferencing the two images. The topographic map uses grid UTM zone 36 grid for northern hemisphere, Projection Transverse Mercator, spheroid Clark 1880 and Datum of Andindan.

2.5.3. GIS database creation and image pre-processing

The common coordinate system used for the data sets is Bikilal, having UTM projection, zone 36 northern hemisphere, 33^0 Central Meridian, Scale factor of 0.9996, datum and ellipsoid of WGS84. The two types of images were georeferenced tie point type using the points that can recognized in the imageries and topographic map of 1:50,000 scale. Using corner pixels of images as control points, ASTER and Landsat TM images were georeferenced in order to be used during rasterize operations, or to create north-oriented (georeferenced) images in resampling of raster maps. The geological map of Ghimbi-Bikilal area was digitized and rasterized. It was used as reference data for crossing operation in statistical descriptive analysis of mean and mean ratio DN-value of the lithology units in each band of the image, for training and validation.

The SWIR bands of ASTER image were resampled to VNIR pixel size using the bicubic algorithm to spatial resolution of 15 m for combining or rationing with the VNIR bands in order to obtain some geologic features from combination of these different channel domains. In the pre-processing stage, histogram analysis of each band was done in order to know the overall DN-value distribution of the image. The haze correction was done using dark-pixel subtraction method for each band in order to remove additive effect of atmosphere because haze results in overall higher DN-values that cause reduction of the contrast in an image. Since vegetation impedes observation of spectral properties (reflectance) of underlying rocks, the vegetation effect has been masked from each band using a threshold value of NDVI (normalized difference vegetation index) before statistical descriptive analysis of DN-value was done for each lithology unit in each image band.

Chapter 3: Multi-spectral Lithologic Remote Sensing

The objective of this chapter is to study whether the different lithologic units in the Ghimbi-Bikilal area are distinguishable from each other based on remote sensing data from the visible to the short-wave infrared region (0.5-2.5μm) of the electromagnetic (EM) spectrum. These data are mostly used in lithologic remote sensing.

3.1. Introduction

Interaction between electromagnetic (EM) radiation and the atoms and molecules that make up the rock or minerals produces vibrational-rotational or electronic processes that create spectral features. Reflectance spectra of minerals and rocks in the visible to short-wave infrared wavelength (0.5-2.5μm) region of the EM spectrum are characterized by absorption features caused primarily by electronic transitions and vibrational transitions (F. van der Meer, 2002) [21]. These diagnostic spectral features can provide a way to detect or identify minerals, to distinguish lithologic units and to determine wall rock alteration products (Michael J. Abrams) [1] by using remote sensing.

Multi-spectral (ASTER and Landsat TM) data sets can contain information about the composition of the rocks of the study area in terms of their spectral response in the visible to SWIR ranges of the electromagnetic spectrum. Image processing methods are applied to multi-spectral data for information extraction and mapping geologic features. The overall methodology of multi-spectral remote sensing of the different lithologic units, especially the apatite-mineralized gabbroic rocks, in the study area is shown in Figure 3.1. PIMA analysis was taken on 20 fresh rock samples that represent the major rock types of the study area in order to have an overall picture of the spectral characteristics and spectral separability of the rocks and it is used to select suitable bands for classification. After image pre-processing (i.e., haze correction, masking of vegetated areas) of the Landsat TM and ASTER data sets, a descriptive analysis of the statistics of the DN values per lithologic unit, according to the published geologic map, is undertaken. This descriptive analytical stage is carried out to determine which of the individual spectral bands or spectral band ratios of the Landsat TM and ASTER data are useful in multi-spectral classification of lithologic units from the remotely-sensed datasets. In addition to this, image transformation such as principal component analysis (PCA) and band ratioing were also done to further determine most suitable bands for lithologic discrimination.

3.2. PIMA analysis

3.2.1. The PIMA instrument

The PIMA (Portable Infrared Mineral Analyzer) is a portable infrared spectrometer, which operates in the SWIR range of the EM spectrum for the analysis of minerals. Some of the applications of PIMA are mineral identification, alteration mapping, remote sensing ground-truthing and lithology mapping. The instrument measures spectra in the 1.3-2.5μm wavelength regions with a 7-10 nm spectral resolution and a 2.5 nm sample interval (Spectral International Inc. (SII) [38]. Reflectance spectra of rock samples could be measured by PIMA in order to have an overall picture of the spectral characteristics of surficial materials and spectral separability of lithologic units and to select areas that are spectrally representative for different rocks that can be detected in the image data. The PIMA data can indicate absorption features in the SWIR, which are due to stretching of bonds OH- (1400 nm, 1550 nm, 1750-1850 nm), Al-OH (2160-2220 nm), H_2O (1400 and 1900 nm), Fe-OH (2230-2295 nm), Mg-OH (2300-2360 nm), CO_3^- (2300-2350 nm) and NH_4 (1870 nm, 1990 nm and 2155 nm). The mineral groups suitable for PIMA analysis are phyllosilicates (clays, chlorite and serpentine minerals), hydroxylated silicates (epidote, amphiboles), sulphates (alunite, jarosite and gypsum), carbonates (calcite, dolomite, ankerites and magnesite) and ammonium bearing minerals (buddingtonite, illite). There are features that make PIMA analysis not very useful, such as broad water bands associated with fluid inclusions and clay absorption due to weathering/alteration of feldspathic components in the samples. There are also some very problematic minerals in mixtures such as opaque minerals (magnetite and sulphides) finely disseminated in a sample and present in

proportions of >5-10%. Due to this, the effect on the spectrum is to lower the reflectance and to weaken the spectral absorption features of other minerals in sample.

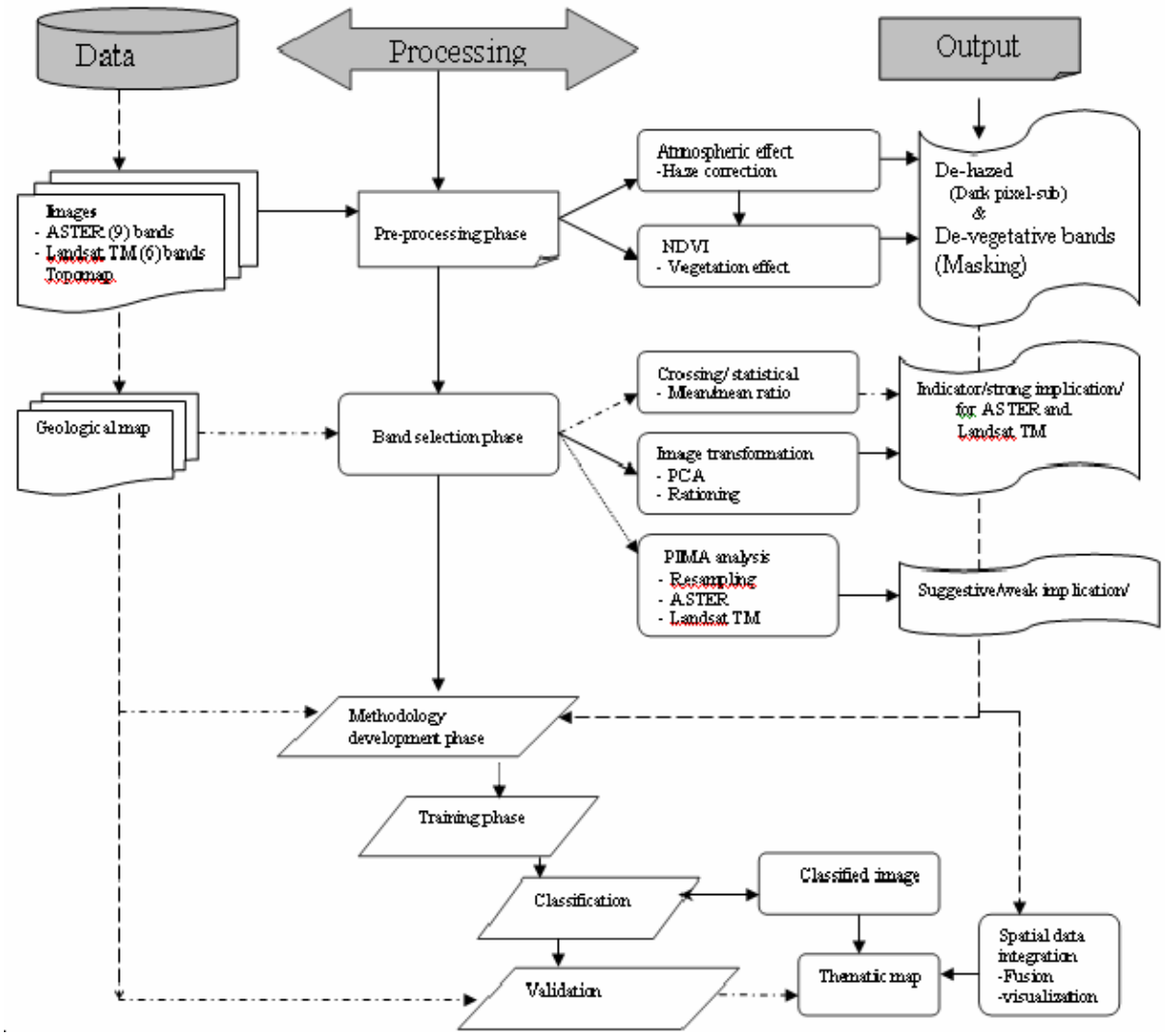

Figure 3.1: Flowchart of methodology for multi-spectral remote sensing of lithologic units in the study area

3.2.2. PIMA measurements

PIMA measurements were done on 20 fresh rock samples that represent the major lithologies in the study area. These rock samples were collected from the field in order to have an idea about the spectral behavior or separability of the major lithologic units. The rock samples can be classified into two major rock groups: (1) BLGC group and (2) country rock group. The BLGC group consists of massive olivine gabbro (MOG), porphyritic olivine gabbro (POG), apatite-magnetite-ilmenite-bearing meta-amphibole gabbro (hbt) and meta-amphibole gabbro (AG). The country rock group consists only of granitic-gneiss (GG). The acronyms given here refer to prefixes of rock sample labels. Each rock sample was measured four times and a total of 80 measurements were obtained.

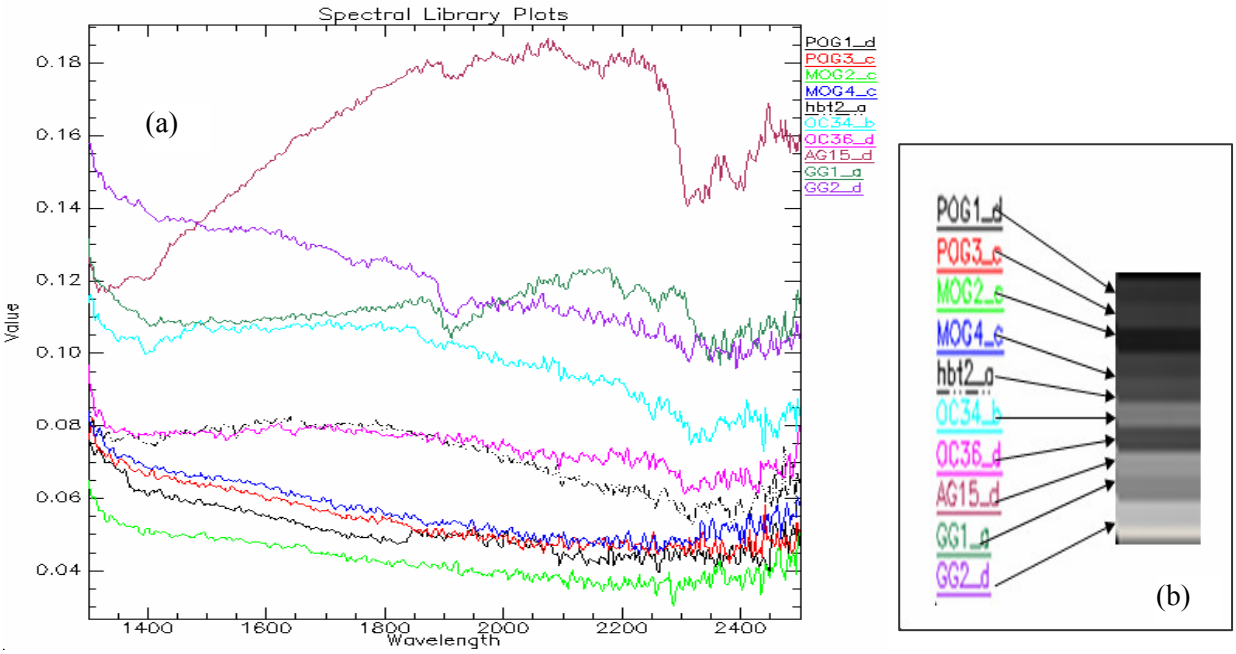

Figure 3.2: (a**)** Spectral reflectance properties of rock samples and (b) spectral slice of the PIMA data corresponding to litho-stratigraphic column

The results of the PIMA measurements, as shown in Figure 3.2, indicate the spectral reflectance properties, stratigraphic column and spectral slice for 10 rock samples that represent the major rocks of Ghimbi-Bikilal area. It is apparent that the porphyritic olivine gabbro (POG), massive olivine gabbro (MOG), meta-amphibole gabbro (hbt) and outcrop (OC) 36 of mineralized zone showed a very low reflectance comparing to other units.

As shown in the Figure 3.2, even though the reflectance is very low and full of noise, samples of granitic-gneiss (GG) show absorption features at 1916 and 2350 nm. Rock samples collected from meta-amphibole gabbro (hbt) and outcrops (OC) 34 and 36 (apatite-ilmenite-bearing meta-amphibole gabbro) show absorption features at 1400 and 2300-2400 nm, whereas samples of porphyritic and massive olivine gabbros (POG and MOG, respectively) show featureless absorption features within this range. In general, rock samples of meta-amphibole gabbro (AG) show at least two types of absorption features, one group with relatively good absorption features between 2300 to 2400 nm and another group without clear absorption feature. Some rock samples such as sample AG15 of meta-amphibole gabbro and olivine gabbro show similar absorption features to diorite and gabbro, respectively, as compared with USGS igneous rock spectral library.

In general, as shown in the Figure 3.2, it is not easy to distinguish between lithologic units in the study area based on the PIMA measurements, since it is almost noisy and featureless absorption features may be a result of low reflectance and the presence of opaque minerals that can weaken the spectral absorption features of other minerals in the rock samples. However, based on clear differences in intensity of reflectance of the rock samples in the SWIR of EM spectrum, it is apparent that the different lithologic units in the area can be spectrally separable or identifiable from each other in multi-spectral datasets. To test this assumption, the PIMA spectral measurements were re-sampled to the spectral band pass of Landsat TM and ASTER (Figure 3.3).

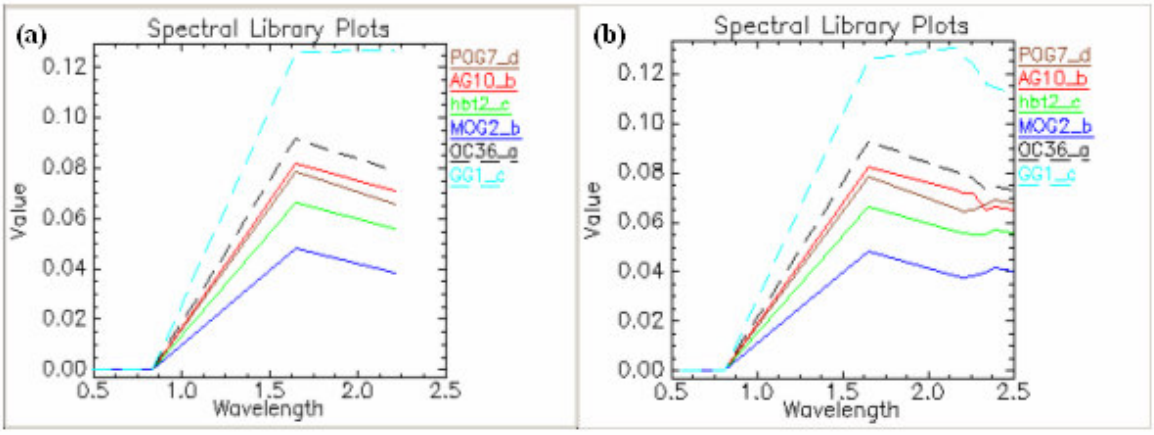

Figure 3.3: PIMA measurements on rock samples re-sampled to band pass of (a) Landsat TM and (b) ASTER

3.2.3. Implications for usefulness of Landsat TM and ASTER spectral bands

The PIMA spectral measurements for some representative of rock samples were re-sampled to Landsat TM and ASTER band pass as shown in the Figure 3.3 in order to determine, which spectral bands of Landsat TM and ASTER imagery can be useful in remote sensing of the different lithologic units in the study area. Based on PIMA spectral data re-sampled to Landsat TM band pass (Figure 3.3a), Landsat TM5 and TM7, and therefore band ratio TM5/TM7, are indicated to be useful in remote sensing of the major lithologic units in the study area. Based on PIMA spectral data re-sampled to ASTER band pass (Figure 3.3b), ASTER bands Rb04, Rb05, Rb06, Rb08 and Rb09, and therefore band ratios Rb04/Rb06, Rb08/Rb06, Rb04/Rb08, Rb07/Rb09 and Rb09/Rb08, are indicated to be useful in remote sensing of the major lithologic units in the study area. These implications of the PIMA analyses will be further studied through descriptive analysis of the DN values of lithologic units in the available Landsat TM and ASTER imageries.

3.3. Descriptive analysis of image data

The following procedures were followed to process the multi-spectral Landsat TM and ASTER images and to study the characteristics of the different lithologic units in the images.

- Analysis of histograms of each spectral band
- Haze correction by dark pixel subtraction method for each band
- Creation of NDVI images
  - For Landsat TM: NDVI=(TM4–TM3)/(TM4+TM3)*127+128
  - For ASTER: NDVI=(Band3–Band2)/(Band3+Band2)*127+128
- Analysis of NDVI images to determine a threshold value for highly vegetated areas
  - For Landsat TM bands a threshold of 175 NDVI was used
  - For ASTER bands a threshold of 135 NDVI was used
- Masking of highly vegetated areas in the de-hazed bands using NDVI threshold values
- Crossing raster map of published geological map with the haze and vegetation masked bands
- Determining the mean and standard deviation of DN values for each lithologic unit in images of individual bands and band ratios
- Creating graphs of mean DN values for each lithologic unit to determine bands or band ratios that are useful in remote sensing the different lithologic units.

3.3.1. DN values of lithologic units in Landsat TM data

Figures 3.4 and 3.5, respectively show the mean DN values for the different lithologic units in images of single bands and band ratios of Landsat TM. In general, all lithologic units show low and

narrow differences between the mean DN values, which are nearly below 50 in bands TM1 to TM4 (Figure 3.4). The lithologic units show wider difference in mean DN values in bands TM5 and TM7. The granitic-gneiss and the meta-amphibole gabbro have slightly higher mean values in TM5 and TM7. In general, the mean values of TM1 are lower compared to mean values of TM3 may be due to strong iron absorption and reflection. The mean values of TM5 are greater than the mean values of TM7, which might be due to strong clay mineral reflection and absorption. In the band ratio images, mean DN values for TM5/TM1 and TM5/TM2 in all lithologic units are high and widely different (Figure 3.5). The prospective gabbro has highest mean DN value in band ratio image TM5/TM2.

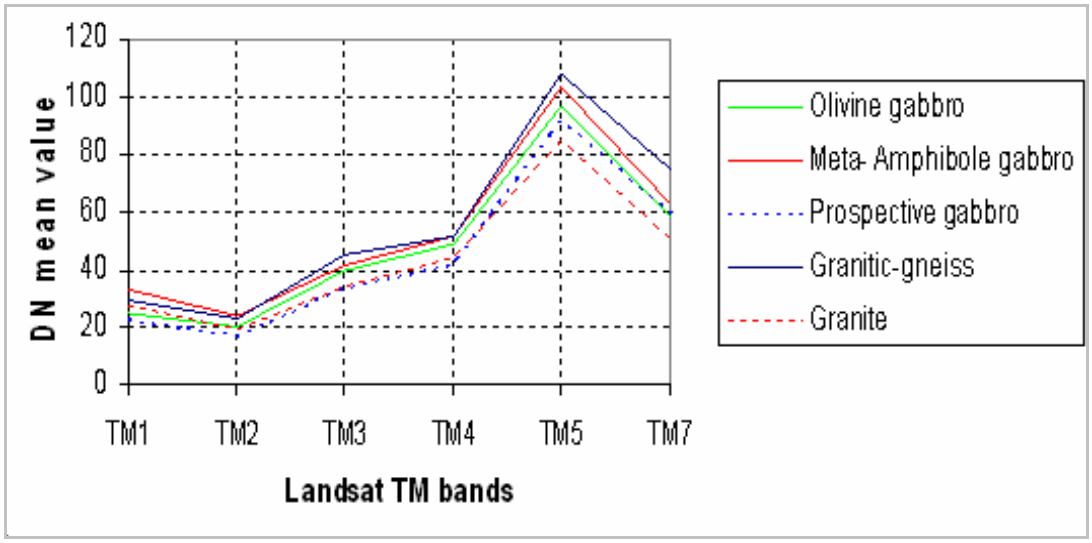

Figure 3.4: Mean DN values of lithologic units in individual spectral bands of Landsat TM data

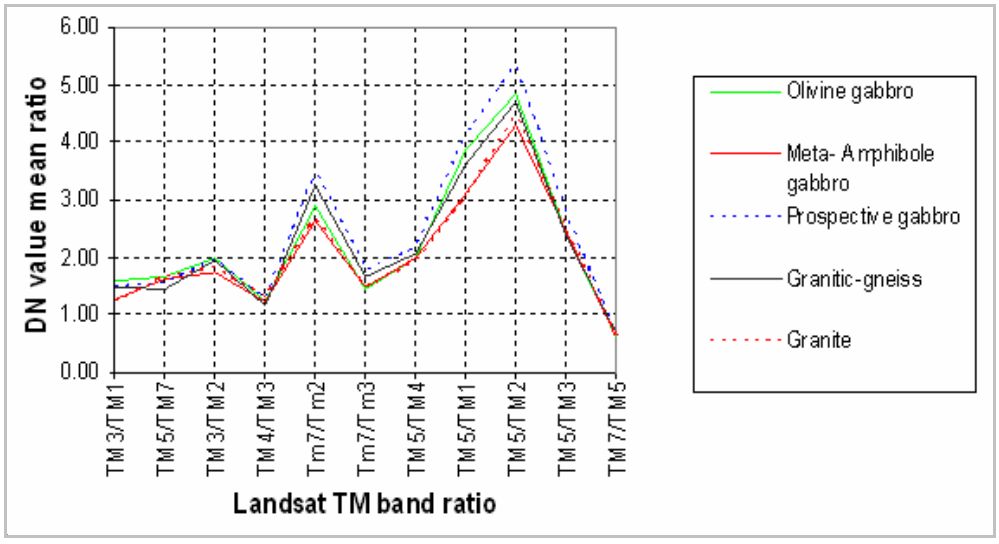

Figure 3.5: Mean DN values of lithologic units in spectral band ratio images of Landsat TM data

3.3.2. DN values of lithologic units in ASTER data

Figures 3.6 and 3.7, respectively show the mean DN values for the different lithologic units in images of single bands and band ratios of ASTER respectively. As shown in Figure 3.6, the granitic-gneiss unit has higher mean DN values than the gabbroic rocks in all single bands. Most of the lithologic units, except the granitic-gneiss, have similar mean DN values in all bands except in Rb01, Rb02 and Rb08. The prospective gabbro has similar mean DN values with the non-prospective

gabbros in all bands. Generally, Figure 3.6 shows that the gabbroic rocks and the granitic-gneiss are distinguishable in the ASTER multi-spectral data.

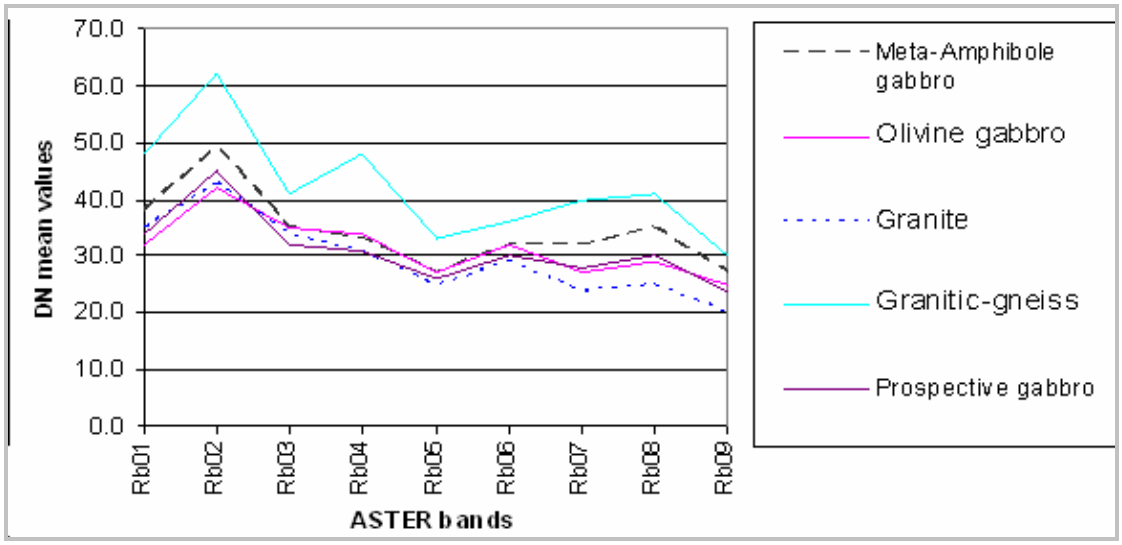

Figure 3.6: Mean DN values of lithologic units in individual spectral bands of ASTER data

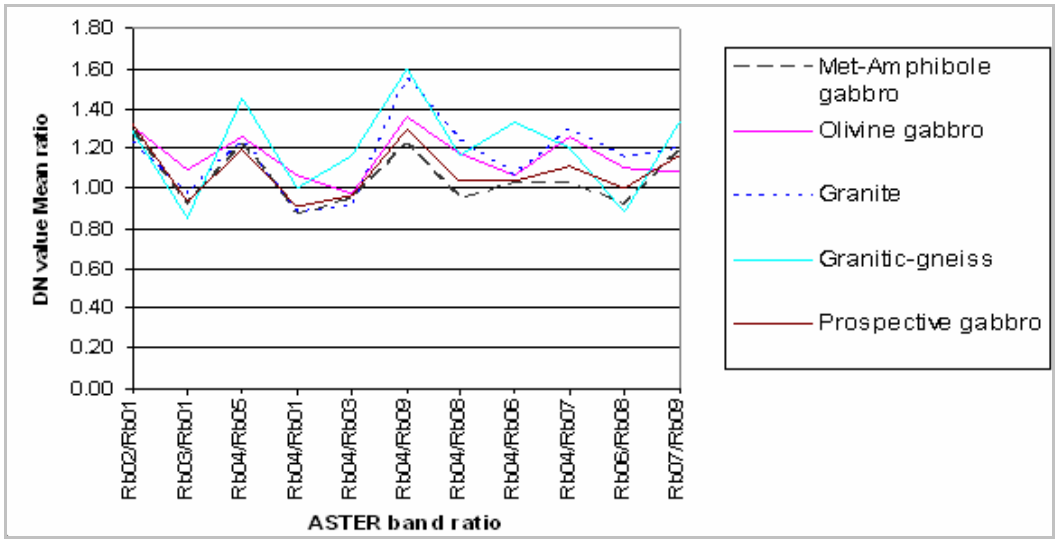

Figure 3.7: Mean DN values of lithologic units in spectral band ratio images of ASTER data

In regard to ASTER band ratios (Figure 3.7), Rb04/ Rb09, Rb04/Rb05, Rb06/Rb08 of ASTER image are the possible band ratios that can be useful to discriminate the major rock types of the area.

3.3.3. Implications for multi-spectral lithologic remote sensing

Generally, as shown in the figures above, TM5, TM7, TM3, TM1 and TM3/TM1, TM5/TM1, TM7/TM2, TM5/TM2 from Landsat TM imagery and Rb01, Rb02, Rb08, Rb04/Rb09, Rb04/Rb05, Rb04/Rb07, Rb06/Rb08 from ASTER imagery are potentially useful in multi-spectral classification of the major lithologic units in the study area. The results of descriptive analysis also suggest that band ratio images rather than individual bands of ASTER data are more useful in multi-spectral classification of the major lithologic units in the area. All these implications from the statistical

analyses of DN values of lithologic units in the Landsat TM and ASTER datasets will be further tested here.

3.4. Image transformation and visualization

3.4.1. Principal components analysis of individual bands

The Principal Component Analysis (PCA) was used for lithologic feature detection from the Landsat TM and ASTER data. PCA is a statistical method that is widely used and useful to produce uncorrelated output bands, to segregate noise components and to reduce the dimensionality of data sets. Since multi-spectral data bands are often highly correlated, the principal component (PC) transformation is used to produce uncorrelated output bands, (Floyd F. Sabins, 1986 [32], (John A. Richards, 1993) [31], (E.J.M. Carranza, 2002, [7]). This is performed by finding a new set of orthogonal axes that have their origin at the data mean and that are rotated so that the data variance is maximized. By using principal components analysis, most of the variance in bands of Landsat TM/ASTER data sets can be explained in two or three components.

3.4.1.1. Principal components analysis for Landsat TM bands

The standard principal component analysis for Landsat TM bands was done using ILWIS software for 6 TM bands excluding the thermal band TM6. The relative weights of the original bands in each component (Table 3.1) are explained as loadings that show correlations in the data original bands. High positive loadings, high negative loadings, and near zero loadings indicate positive correlation, negative correlation and lack of correlation in the data in the original bands, respectively.

Table 3-1: Loadings of the different bands in each PC component for Landsat TM data

	TM1	TM2	TM3	TM4	TM5	TM7	Variance (%) per band
PC1	0.16	0.123	0.247	0.359	0.768	0.425	96.88
PC2	0.037	0.13	0.24	0.621	0.01	-0.734	1.72
PC3*	0.677	0.324	0.391	0.038	**-0.472**	**0.245**	0.94
PC4	0.051	0.142	0.504	-0.683	0.335	-0.381	0.30
PC5	**-0.674**	0.042	**0.615**	0.124	-0.274	0.276	0.15
PC6	-0.242	0.917	-0.312	-0.05	0.023	0.007	0.02

N.B. * negated image

The PC1 explains 96.88 % of the total variance and has positive loadings from all bands with highest loading in TM5 (0.768) and TM7 (0.425). The first PC is generally a weighted average of all data and represents albedo and topography effect found in the scene (S.A. Drury, 1993) [16]. The PC2 accounts for 1.72% of the total variance and has high positive loading in TM4 (0.621), low positive loading in TM3 (0.24) and high negative loading in TM7. The PC2 represents the effect of vegetation.

The PC3, which accounts for 0.94% of the total variance, has high positive loading in TM1 (0.677), negative loading in TM5 (-0.472) and low positive loading in TM7 (0.245). The PC3 possibly represent presence of clay-rich zones because of opposite signs of loadings in TM5 and TM7 (Crosta, A.P. and Rabelo A., 1993) [12]. When this component is multiplied by -1, clay zones will appear as bright pixels in the image, because clays should have bright reflection pixels in TM5 and dark pixels absorption in TM7 (Figure 3 .8).

The PC4 explains 0.3% of the total variance and has high positive loading in TM3 (0.504) and very low positive loading in TM1 (0.051). This represents presence of iron-oxide zones (Crosta, A.P. and Rabelo A., 1993) [12]. The PC4 has also positive loading in TM5 and negative loading in TM7, which represents presence of clay zones. So PC4 possibly represents overlap between iron oxide zones and clay zones.

The PC5 explains 0.15% of total variance and has high negative and high positive loadings in TM1 and TM3, respectively and this implies presence of iron oxide zones. The PC6 explains 0.02% of the total variance, and has very high positive loading in TM2 (0.917) and low and negative loadings for the rest bands. The PC6 probably represents zones that were masked due to high NDVI values reflecting dense vegetation. In general, results of the PCA suggest useful bands and band ratios to be

TM1, TM3, TM5 and TM7 and TM5/TM7, TM5/TM1, TM5/TM2, TM5/TM3, TM5/TM4 and TM3/TM1.

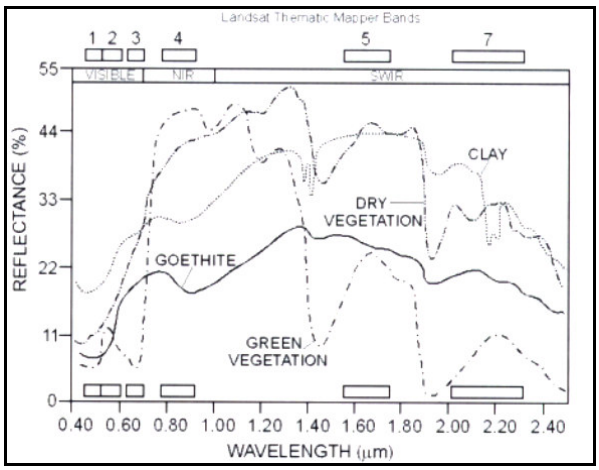

Figure 3.8: Typical reflectance spectra of Landsat TM for vegetation, iron oxides and clays (from Fraser and Green, 1987)

To extract lithologic information from the Landsat TM data based on the results of Principal Component Analysis (PCA), the PC3, PC4 and PC5 were selected for making a color composite (Figure 3.9) to map zones of clay and iron oxide. The color composite image is formed by assigning PC3 as red for clay variation, PC4 as green for iron and clay overlap zones and PC5 as blue for iron variation. Even though the total variances of PC3, PC4 and PC5 are very low, the color composite image PC3-4-5 (RGB) shows at least four main lithological units that can be discriminated well since they contain high reflectance and absorption features for iron and clay variations.

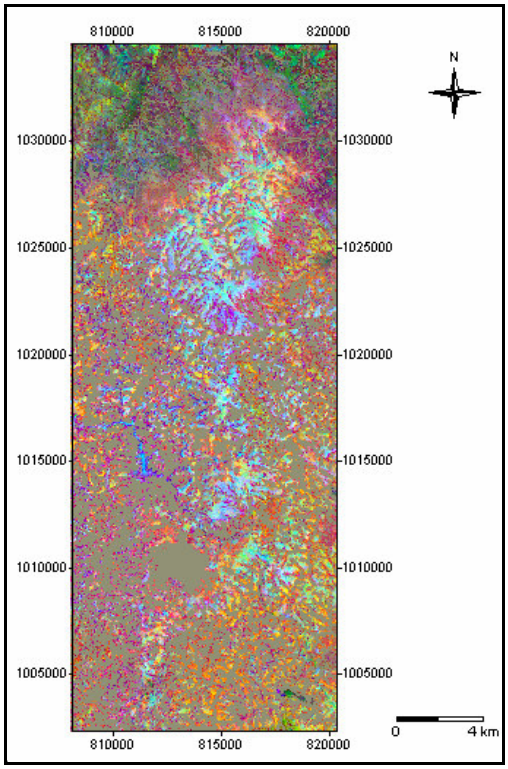

Figure 3.9: Colour composite Landsat TM PC 3-4-5 (RGB)

The mineralogical compositions of the major rocks found in the study area based on the literature review of the regional geological works are as follow. The olivine gabbro is composed of plagioclase,

pyroxene, olivine, biotite and opaque minerals. The meta-amphibole gabbro is composed of mainly of plagioclase and amphiboles (hornblende, tremolite, actinolite) and some accessory minerals such as chlorite, epidote, muscovite, sericite and sphene. The prospective gabbro consists of meta-amphibole gabbro and mainly the minerals are plagioclase and amphibole varieties in addition to the economic minerals (apatite, ilmenite and magnetite). The granitic-gneiss is mainly composed of k-feldspar, quartz, plagioclase, hornblende, micas and some epidote and chlorite.

As shown in Figure 3.9, the light blue-cyan color shows areas covered by the well exposed unit that is mapped as olivine gabbro and part of meta-amphibole gabbro in the published geological map and runs almost north-south direction. The purple to reddish brown color represents areas covered by the prospective gabbro and part of meta-amphibole gabbro in north, NE and NW of the area forming half-circle like shape surrounding the olivine gabbro unit of the northern part as shown in the geological map of the area. The green color represents areas covered by the granitic-gneiss of the northeastern and extreme northwestern part of the area, which is mapped as meta-amphibole gabbro. The area covered by granitic-gneiss in south and southeastern extreme in the geological map is shown by yellowish color. The SSW and the SSE parts of the study area that is mapped as granitic-gneiss can be discriminated into sub-units.

3.4.1.2. Principal components analysis for ASTER bands

Similarly, principal component analysis was done for nine bands of ASTER. The relative weights of the original bands in each component (Table 3.2) are explained as loadings that show correlation between original bands.

Table 3-2: Loadings of the different bands in each PC component for ASTER data

	Rb01	Rb02	Rb03	Rb04	Rb05	Rb0 6	Rb07	Rb08	Rb09	Variance (%) per band
PC1	0.302	0.401	0.345	0.384	0.298	0.354	0.311	0.321	0.259	96.93
PC2	0.500	0.474	0.364	-0.131	-0.204	-0.232	-0.308	-0.347	-0.256	2.02
PC3*	0.414	0.253	-0.598	**-0.561**	**0.080**	0.076	0.130	0.208	0.144	0.71
PC4	0.277	-0.052	-0.521	0.555	0.141	0.263	-0.108	-0.313	-0.376	0.19
PC5*	**0.506**	**-0.695**	0.291	-0.223	0.202	0.246	-0.097	-0.091	0.088	0.06
PC6	0.353	-0.251	-0.030	0.238	-0.419	-0.458	0.459	0.342	-0.204	0.03
PC7	-0.166	0.044	0.181	-0.313	0.206	0.253	0.339	0.111	-0.778	0.02
PC8	-0.027	0.014	0.022	-0.050	-0.763	0.638	0.044	-0.034	0.051	0.02
PC9	-0.029	0.022	0.009	-0.075	0.038	-0.064	0.666	-0.705	0.218	0.01

N.B. * negated image

The PC1 explains 96.93 % of the total variance and has positive loadings in all bands. The PC1 is generally is a weighted average of all data and represents albedo and topography effects in the scene.

The PC2 accounts for 2.02% of the total variance and has high positive loading in Rb01, Rb02 and Rb03 and negative loadings in the rest bands. The PC2 represents differences in spectral characteristics of surficial materials in the VNIR and in the SWIR bands.

The PC3, which explains 0.71% of the total variance, has positive loadings in Rb01 (0.414) and Rb05 (0.080) and high negative loadings in Rb03 (-0.598) and Rb0 4 (-0.561). If PC3 is negated, the image can show bright pixels implying presence of clay minerals.

The PC4, which accounts for 0.19% of the total variance, has high positive loading in Rb04 (0.555) and low positive loading in Rb05 as well as negative loading in Rb02 (-0.052). The PC4 also possibly implies presence of clays as it shows high reflectance in Rb04 and low reflectance in the other bands.

The PC5 explains 0.06% of the total variance and has positive loading in Rb01 (0.506) and negative loading in Rb02 (-0.695). This suggests presence of iron oxides since band 2 and band 1 have opposite signs. This component was multiplied by -1 (negating), to map iron zone as bright pixel and this PC was used in making color composite image.

The PC6, which accounts for 0.03% of the total variance, has positive loadings in Rb01, Rb04, Rb07, Rb0 8 and negative loadings in Rb02, Rb03, Rb05 and Rb06. In general, PC6 possibly represents overlap between clay and iron oxide zones (see Table 3.2).

The PC7, which accounts for 0.02% of the total variance, has low positive loadings in Rb05, Rb06, Rb07 and highest negative loading in Rb09 (-0.778). The PC8 explains 0.02% of total variance with highest positive loadings in Rb06 (0.638) and negative loading in Rb05 (0.763). The PC9, which explains 0.01% total variance, has highest loading in Rb07 (0.666) and low and negative loadings in the other bands. It is difficult to interpret what PC7, PC8 and PC9 represent. In general, results of PCA of ASTER data indicate that PC3, PC5 and PC6 can give geological information. This suggests further that the potentially useful bands and band ratios are Rb01, Rb02, Rb04, Rb05, Rb03, Rb09, Rb06 and Rb04/Rb05, Rb02/Rb01, Rb04/Rb03, Rb04/Rb02, Rb04/Rb06, Rb04/Rb09.

In order to extract lithologic information of the study area from the PCA of the ASTER data, the geologically meaningful PCs were selected in terms of their indications for the presence of clay and iron oxide in the surficial materials in the study area. Therefore, a RGB color composite image (Figure 3.10) was created by assigning PC3 as red for clay variation, PC6 as green for clay and iron overlaps, and PC5 as blue for iron variations. Characteristic of some alteration minerals in ASTER is shown in Figure.11.

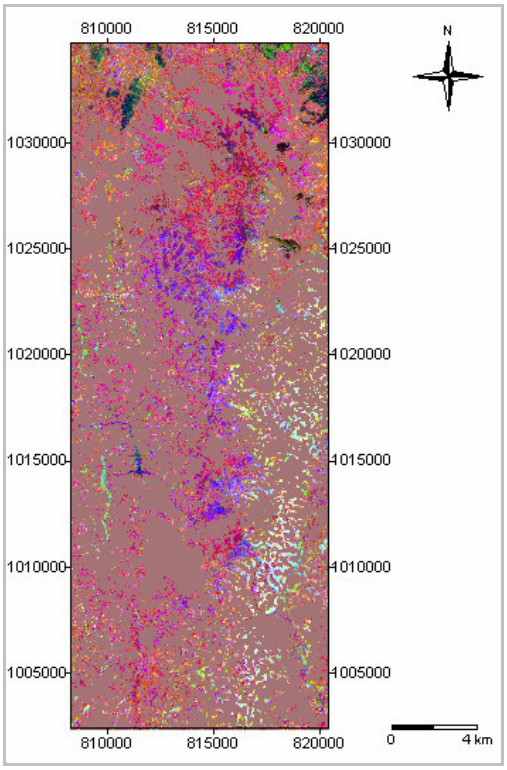

Figure 3.10: Color composite of ASTER PC 3-6-5 (RGB)

As shown in Figure 3.10, the central part, which is mapped as olivine gabbro mainly composed of iron bearing minerals (pyroxene and olivine), is clearly indicated by blue to purple pixels. The image shows that, even though the olivine gabbro, which is mapped as one unit in the geological map, can probably be differentiated into two sub-units. The prospective gabbro, as shown in the geological map, is indicated by bright-pink pixels in the composite image, almost making as ring-like zone around the olivine gabbro in the northern part of the area. The NNW extreme part of the study area, which was mapped as meta-amphibole gabbro and granitic-gneiss separately, but in this image it is almost similar. Areas covered by granitic-gneiss in southeastern and eastern part of the area are shown as cyan-light-green color. The meta-amphibole gabbro, which is mapped in the central and western part, is shown as reddish brown and it is clearly discriminated from the olivine gabbro. In general, this PC composite image discriminates well the central part of the study area which is mapped as olivine

gabbro, the granitic-gneiss mapped in eastern, south-eastern and south, prospective gabbro and meta-amphibole gabbro of the central part of study area.

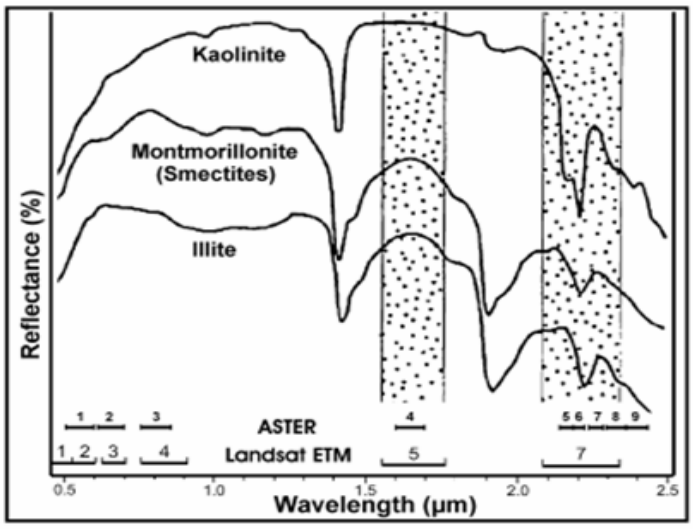

Figure 3.11: Spectral of some alteration minerals showing their characteristic absorption peaks, and wavelength intervals of Landsat ETM and ASTER bands (after Raul Pablo Andrada de Palomera, 2004; modified from Sabins, 1999)

3.4.2. Band ratio images for Landsat TM and ASTER

The band ratio method can be used in order to enhance spectral differences between bands and to reduce the effects of shadowing and illumination variations caused by differences in ground slope. In band ratio, dividing one spectral band by another produces an image that provides relative band intensities or enhances subtle difference in spectral reflectance that is a characteristic for rocks and soils (Floyd F. Sabins, 1986) [32], (John A. Richards, 1993) [31], F. van der Meer, 2002) [21]. Three ratio images can be combined into a color-ratio-composite (CRC) image to determine the approximate spectral shape for each pixel's spectrum. Even though, a band ratio is simply a numerator band divided by a denominator band, to calculate useful band ratios, the useful numerator and denominator bands were selected based on the PIMA analysis, statistical descriptive analysis and PCA of the image datasets.

3.4.2.1. Band ratio of Landsat TM bands

The potentially useful bands and band ratios of Landsat TM data for discrimination of the rocks in the study area based on the PIMA analysis, statistical descriptive analysis of the mean and mean ratio DN-value of lithology and the PCA of 6 TM bands are summarized as:

- From PIMA analysis (1.3-2.5 μm)-TM5, TM7, and TM5/TM7.
- From statistical descriptive analysis of band mean and band ratio mean DN-values of each lithologic unit in images of individual bands and band ratios
  - Single bands -TM7,TM5 ,TM3 and TM1
  - Band ratios - TM7/TM2,TM5/TM2,TM5/TM1,TM3/TM1
- From PCA of six TM bands (excluding thermal band TM6)
  - Single bands - TM5,TM7, TM4, ,TM3, TM1
  - Band ratios -TM5/TM7, TM3/TM4, TM5/TM4 ,TM3/TM1, TM4/TM3
    - Band ratio TM5/TM7 as indicator for clay variations
    - Band ratio TM3/TM1 as indicator for iron variations and the other band ratios as indications of overlaps between iron and clay zones.

Band ratio of TM3/TM1 enhances contribution of iron minerals since reflectance and absorption of iron occur at TM3 and TM1, respectively (S.A. Drury, 1993), [16]. In addition to this, band ratio TM5/TM4 can also show iron variation due to crystal field effect. The implication of TM5/TM7 is for

clay-rich minerals, which have high reflectance in TM5 and low value in band TM7 due to the hydroxyl molecular bonds in minerals stretch and the resultant electronic vibration causes absorption of energy around 2.2μm.

The band ratios TM5/TM2 and TM5/TM1 are helpful for mapping granites, (Hurtado, 2004) [24] and to emphasize mafic igneous rocks, (Jennifer Inzana, et al., 2003) [29]. This may show the variability of Fe in minerals/rocks having broad spectral reflectance features. For instance, the band ratio TM5/TM2 and TM5/TM1 may enhance the spectral differences of such as minerals hydroxyl-apatite and ilmenite, since they have a broad spectral reflectance starting from around 0.5- 2.0 μm as shown in USGS spectral library description. The broad reflections for hydroxyl-apatite suggest poor crystallinity and/or compositional heterogeneity. The very broad spectral feature of ilmenite extending from 0.5μm into the infrared with a maximum at 2.0 μm is due to crystal defects, the presence of impurities, as well as conduction bands due to the iron and titanium extending out from the ultraviolet into the visible, (speclab.cr.usgs.gov) [25]. The possible TM band ratios and their relative spatial feature in the study area are displayed in the following figures for comparison (Figure 3.12). As shown in the different band ratio images, some spatial features and surficial materials are accentuated if the bands used are chosen to cover the peaks, absorption troughs and changes in slope on the curve of spectral signature, (S.A. Drury, 1993) [16].

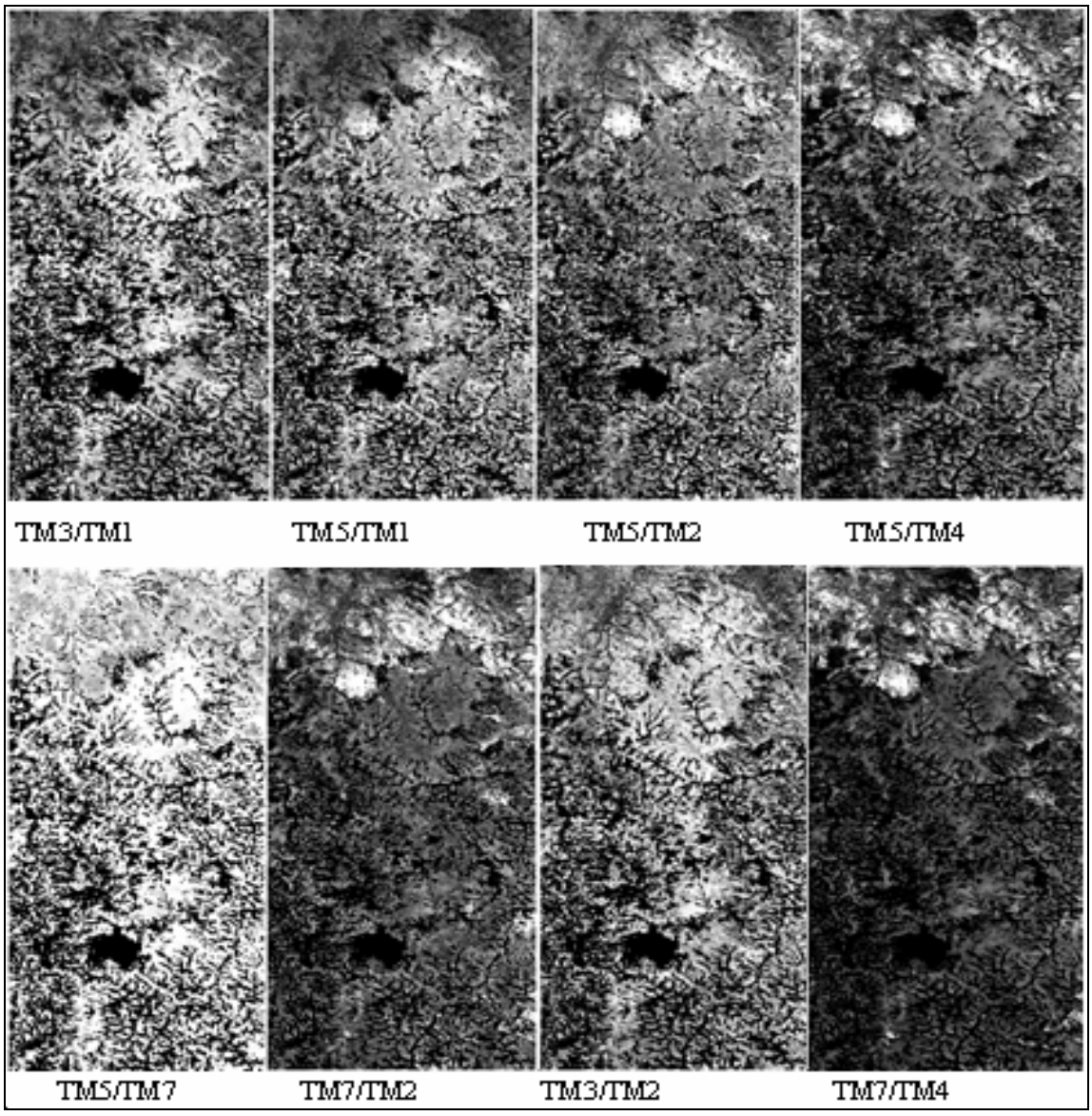

Figure 3.12: Different TM band ratios showing their spatial features in the scene

From visual comparison of the band ratio images, the most suitable band ratio images for lithologic mapping and delineation of known mineralized zones are TM3/TM1, TM5/TM1, TM5/TM2, and TM7/TM2. TM3/TM1 highlights the olivine gabbro in the central part of the area. It also shows that the northern parts of the area are underlain by different lithology than those in the eastern and western parts the area. This inference is based on the darker spectral contrast and smoother topographic expression of pixels in the northern parts, as compared to the brighter spectral contrast and rougher topographic expression of pixels in the eastern and western parts of the area. TM5/TM1 is more or less similar to TM3/TM1, but it shows that pixels of the western parts have slightly darker contrast than the pixels in the eastern parts, which suggest that these areas are probably underlain by different lithologies. TM5/TM1 also accentuates the bright pixels in the known mineralized zone. TM5/TM2 accentuates the known mineralized zone as bright pixels and also accentuates differences in spectral contrast and in topographic roughness of the northern parts as compared to other parts of the area. TM7/TM2 clearly indicates the northern mineralized zones and shows the northern parts to have brighter contrast as compared to other parts of the area. The band ratios images considered most suitable for lithologic interpretation were then combined into two to create color ratio composites of TM7/2-5/1-3/1 and TM7/2-5/2-3/1 (RGB) as shown in Figure 3.13a and Figure 3.13b, respectively.

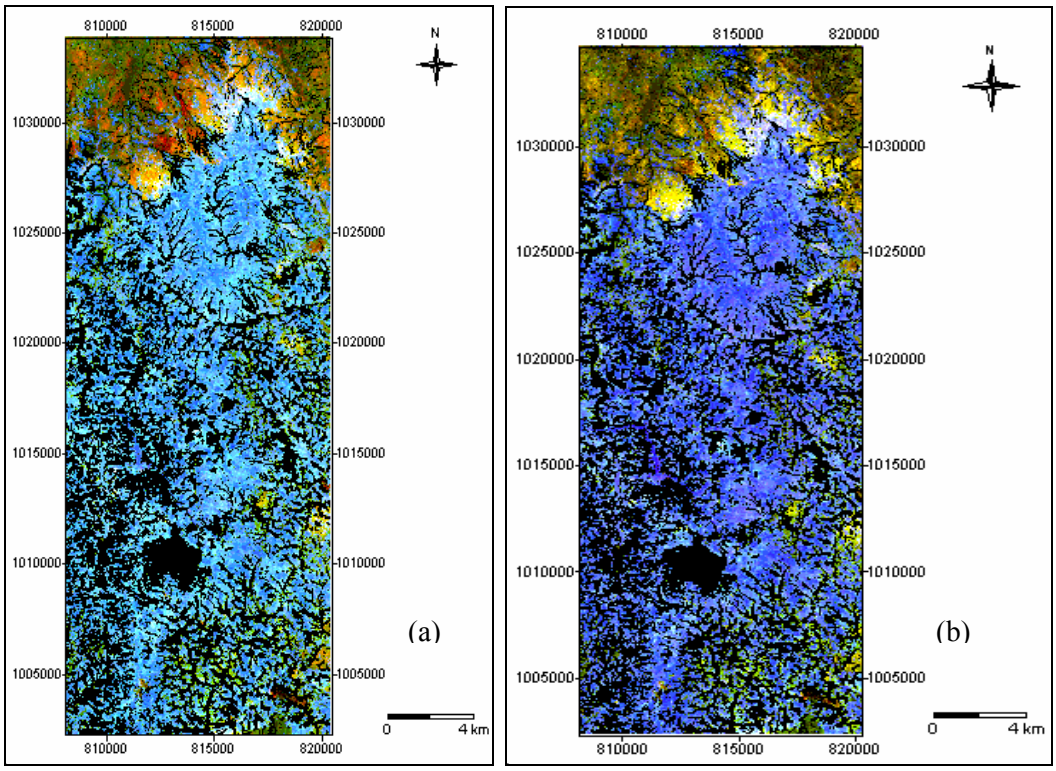

Figure 3.13: Color composite (a) TM 7/2-5/1-3/1 (RGB) and (b) TM 7/2-5/2-3/1 (RGB)

At least three major geological features can be discriminated from the image, in Figure 3.13a, as denoted by color variations in blue-cyan, bright yellow-orange and red-brown pixels. In Figure 3.13b, the different major units are also explained by blue, bright yellow and dark yellow-orange pixels. The area indicated by the bright yellow color in both images covers the spatial features of prospective gabbro as indicated in the published geological map. The band ratio color composite images suggest the presence of at least two lithologic groups. One group, which represents mapped units of granite/granitic-gneiss and meta-amphibole gabbro, occupies the northernmost parts of the area. The other group, which represents mapped units of olivine gabbro, meta-amphibole gabbro and granitic-gneiss, occupies the other parts of the area. A third group, which represents the prospective gabbro, is situated between the first two groups. The bright yellow to bright orange pixels, which represent the third group, indicates enrichment in Fe-O and OH-bearing minerals or rocks or denotes areas of rock alteration and mineralization. The band ratio color composite images show that lithological

discrimination is enhanced in the northern part. The band ratio color composite images suggest that the rest of the study area is covered by almost by one unit (class) except for some smaller and different features in the extreme SSE and SE parts of the area, which were mapped previously as granitic-gneiss in the published geological map. Generally, the results of band ratioing method for Landsat TM data indicate the followings:

- The presence of distinct spectral features, representing major lithologic units, is detectable using TM3/TM1, TM5/TM2, TM5/TM1 and TM7/TM2.
- The color composite image, based on TM7/TM2, TM5/TM2 (or TM5/TM1), and TM3/TM1 in Red, Green and Blue channels, respectively, enhances mainly hydroxyl- and iron-oxide-bearing minerals/rocks.
- Spectral anomalies of mineralized rocks are displayed in bright yellow pixels in the band ratio color composite images (Figure 3.13).

3.4.2.2. Band ratio of ASTER bands

The potentially useful bands and band ratios of ASTER data for discrimination of the rock units in the study area based on the PIMA analysis, statistical descriptive analysis of the mean and ratio mean DN-values of each lithology and PCA results of 9 ASTER bands are summarized as:

- From PIMA analysis (1.3-2.5 μm) - Rb04, Rb05, Rb06, Rb08, Rb09 and Rb04/Rb06, Rb08/Rb06, Rb04/Rb08, Rb07/Rb09 and Rb09/Rb08.
- From statistical descriptive analysis of band mean and band ratio mean DN-values of each lithologic unit in images of individual bands and band ratios
  - Single bands – Rb08, Rb02, Rb01
  - Band ratios – Rb04/Rb05, Rb04/Rb09, Rb06/Rb08, Rb04/Rb07
- From PCA of nine ASTER (VNIR-SWIR) bands
  - Single bands – Rb01, Rb02, Rb04, Rb05, Rb06, Rb08, Rb09 , ,
  - Band ratios – Rb04/Rb05, Rb04/Rb06, Rb08/Rb06, Rb04/Rb03, Rb04/Rb09, Rb04/ Rb07, Rb02/ Rb01.
    - Band ratio Rb04/Rb05 as indicator for clay variations.
    - Band ratio Rb02/Rb01 as indicator for iron variation and the other band ratios as indication overlaps between clay and iron zones.

However, the band ratio images and band ratio color composite images of the ASTER data did not produce better results as compared to the Landsat TM data. This confirmed unseen observation of better results from the Landsat TM single band data (Figure 3.9) as compared to the poor results of the ASTER single band data (Figure 3.10).

3.5. Multi-spectral image classification

Image classification is a method that converts the image data to thematic data. In general, multi-spectral classification is grouping of features, which resemble each other, and separation of unlike ones, and finally to derive an output denoting ground cover and surface characteristics and to recognize anomalous patterns in the image data set. In this research, a supervised type of classification was used based on the selected potentially useful bands or band ratios. The objective of using supervised classification process was to categorize all pixels in a digital image into five lithology classes and from this data, finally to produce thematic map of the area.

The maximum likelihood classification (MLC) including the prior probability, were chosen over other classifications methods to assist in the classification of overlapping signatures. This is because MLC assigns pixels in the images to the class of highest probability and it also considers the cluster center, shape, size and orientation (generally class variability) by calculating a statistical distance based on the mean value and covariance matrix of the clusters (Lucas L.F. Janssen and Gerrit C., 2001), [30].

3.5.1. Image classification for Landsat TM bands

3.5.1.1. Image classification for each band

The Landsat TM multi-spectral data were used to perform the classification based on the spectral pattern present within the data. Based on the implication of PIMA analysis, statistical descriptive analysis and PCA of TM bands, the TM7, TM5, TM3 and TM1 were used as image variables and tested using maximum likelihood classification. Five types of classes similar to the published geological map were used for the training sites. The main aim was to identify examples of the information classes (lithology type) of interest in the image. Before doing classification, a sample set was prepared with five classes consisting of 3532 training pixels. The total number of training pixels used for granite, olivine gabbro, meta-amphibole gabbro, prospective gabbro and granitic-gneiss were 513, 810, 754, 672 and 783, respectively. The image processing software system used develops a statistical characterization of the reflectance for each information class. This stage is often called signature analysis and may involve developing a characterization as simple as the mean or the range of reflectance on each bands, or as complex as detailed analyses of the mean, variances and covariance over all bands. Once a statistical characterization has been achieved for each information class, the image is then classified by examining the reflectance for each pixel and making a decision about which of the signatures it resembles most (Eastman, 1995) [17].

Maximum likelihood classification (MLC) for sample sets containing image variables of TM7-TM5-TM1, TM7-TM3-TM1 and TM7-TM5-TM3-TM1 showed some reasonable lithological feature patterns. In addition to these, classification using prior probability was done for these sample sets in order to favor for some classes over other classes after creating a value column in the table having the same domain as the sample set. The column created contains a prior probability value for each class, in this case the area coverage (%) of each class within the area.

The classification accuracy (%) for the different classes in different image variables were evaluated and plotted as shown in Figure 3.14. The classification accuracy is defined as the proportion of correctly allocated training samples against miss-allocated training samples, (Ernst M. Schetselaar, et al., 2000) [20]. As shown in Figure 3.14, using maximum likelihood classification, the granite (GRT) and olivine gabbro (OLG) have more than 50% and 35-42% classification accuracy, respectively for the different TM band combinations used as image variables. The prospective gabbro (PRG) also showed more than 37% of classification accuracy. The granitic-gneiss (GGn) showed very low classification accuracy in all image variables. The overall classification accuracy is higher in image variable TM7-TM3-TM1 than for other image variables used.

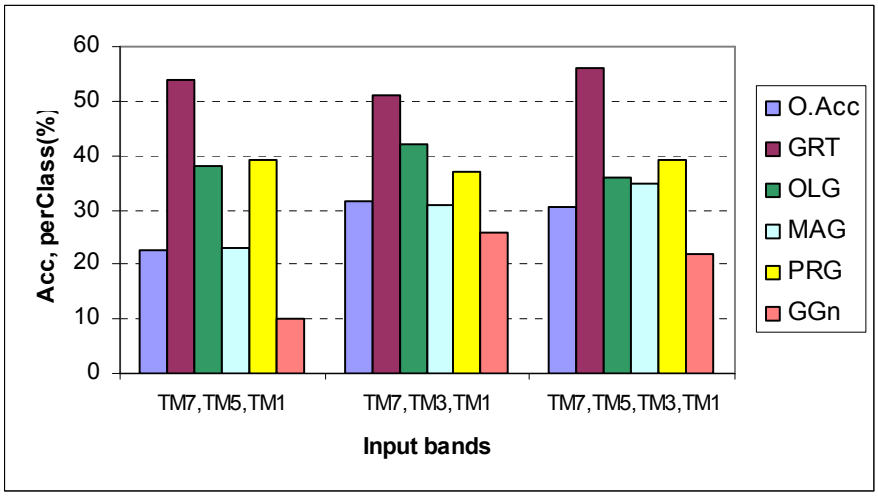

Figure 3.14: Classification accuracy for each lithology class using various TM band variables in MLC. (O.Acc = overall accuracy, GRT = granite, OLG = olivine gabbro, MAG = meta-amphibole gabbro, PRG = prospective gabbro and GGn = granitic-gneiss)

In the prior probability classification (PPC) (Figure 3.15), the classification accuracy for meta-amphibole gabbro (MAG) is more than 40% and prospective gabbro (PRG) is 24-28%, which is lower than in the maximum likelihood classification. The classification accuracy for granitic-gneiss (GGn) however, has increased as compared to the results of MLC. In general, the PPC showed a relatively good improvement in overall classification accuracy, which is 4-7% higher than for the MLC.

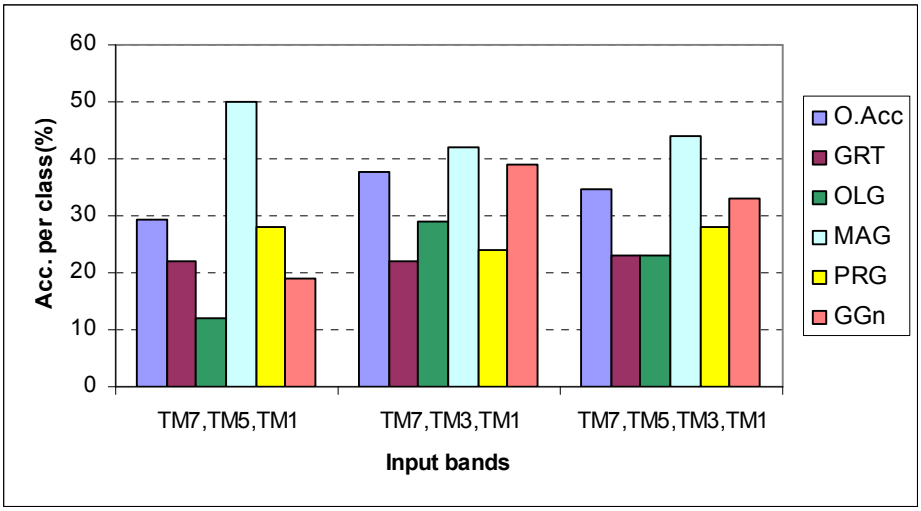

Figure 3.15: Classification accuracy (%) for each lithology class using various TM bands variable in PPC. (O.Acc = overall accuracy, GRT = granite, OLG = olivine gabbro, MAG = meta-amphibole gabbro, PRG = prospective gabbro and GGn = granitic-gneiss)

The classified image by MLC using input bands of TM7, TM5, TM3 and TM1 (Figure 3.16) has a good pattern of lithologic units with reference to the published geological map and as compared to the other classified images. The confusion matrix result showed an overall and average classification accuracy of 30.62% and 37.46%, respectively.

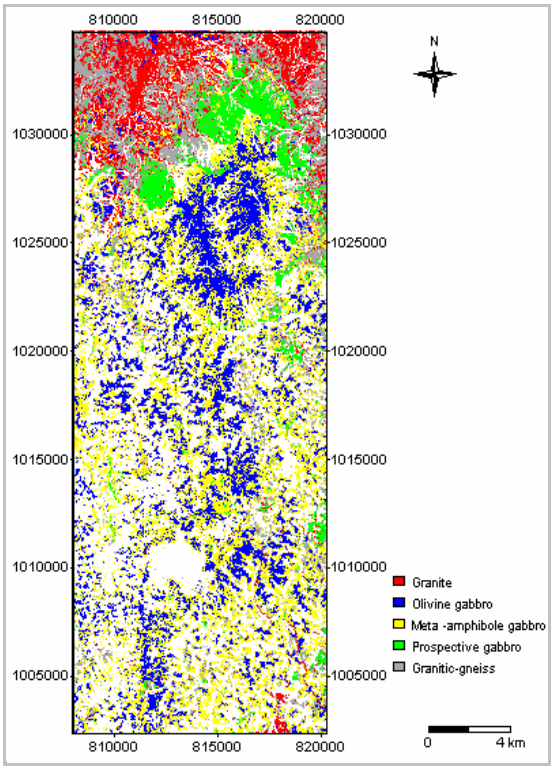

Figure 3.16: Classified image by maximum likelihood using input bands TM1, TM3, TM5 &TM7

3.5.1.2. Image classification for TM band ratios

Band ratios TM5/TM7, TM7/TM2, TM5/TM1, TM5/TM2 and TM3/TM1 were selected based on statistical descriptive analysis and PCA and used as input bands to image classification.

As shown in Figure 3.17, using MLC, the granite (GRT) and olivine gabbro (OLG) have more than 58% classification accuracy almost for all TM band ratios used as inputs. The prospective gabbro (PRG) showed more than 30% of classification accuracy by using as inputs TM7/2-TM5/2-TM3/1 and TM7/2-TM5/2-TM3/1, but has only 24% classification accuracy by using as inputs TM5/7-TM5/1-TM3/1. The granitic-gneiss (GGn) has very low classification accuracy in all classifications. In general, in this classification the olivine gabbro, granite and prospective gabbro have higher classification accuracy as compared to the other lithologic units, but the overall accuracy is only about 20%.

The classified images using MLC of the TM band ratios TM7/2-TM5/2-TM3/1 and TM7/2-TM5/2-TM3/1 are shown in Figure 3.18a and 3.18b, respectively. These two classified images show properly the distribution of the acidic rocks (granite/granitic-gneiss), basic rocks (olivine gabbro) and prospective gabbro.

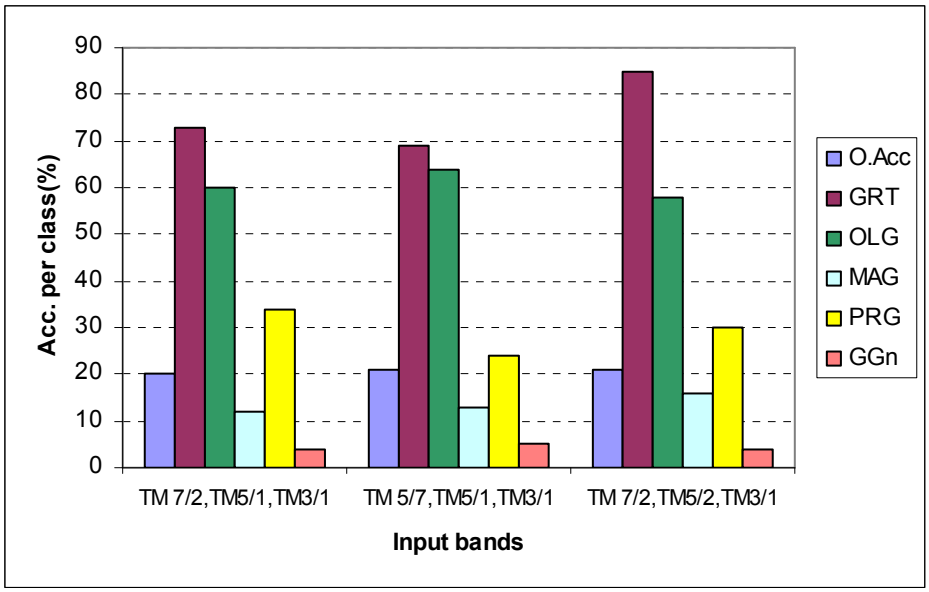

Figure 3.17: Classification accuracy (%) for each lithology class using band ratios as inputs to MLC. (O.Acc = overall accuracy, GRT = granite, OLG = olivine gabbro, MAG = meta-amphibole gabbro, PRG = prospective gabbro and GGn = granitic-gneiss)

3.5.2. Image classification for ASTER bands

A sample set was prepared with five classes consisting of total 41857 training pixels for five classes. The number of training pixels for granite, olivine gabbro, meta-amphibole gabbro, prospective gabbro and granitic-gneiss were 2285, 9893, 13474, 5334 and 10871, respectively.

3.5.2.1. Image classification using each ASTER band

For image classification purpose, Rb01, Rb02, Rb03, Rb04, Rb05, Rb06, Rb08 and Rb09 were used since these are considered the suitable bands based on the results of the statistical descriptive analysis and PCA. The classification accuracy for each class based on MLC is shown in figure 3.19. The olivine gabbro (OLG) has good classification accuracy relative to other units in all combinations of input bands used in this classification. The classification accuracy for prospective gabbro (PRG) is 31% based on input bands Rb08, Rb05, Rb04, which resulted in a classified image with an overall and average classification accuracy of 34.72% and 36.06%, respectively. The classified image (Figure 3.20) shows more distribution of olivine gabbro occupying the central part of the area. The prospective gabbro also covers more area in the northern part of the area as compared with its smaller

area coverage in the published geological map. The granitic-gneiss also has relatively good area coverage.

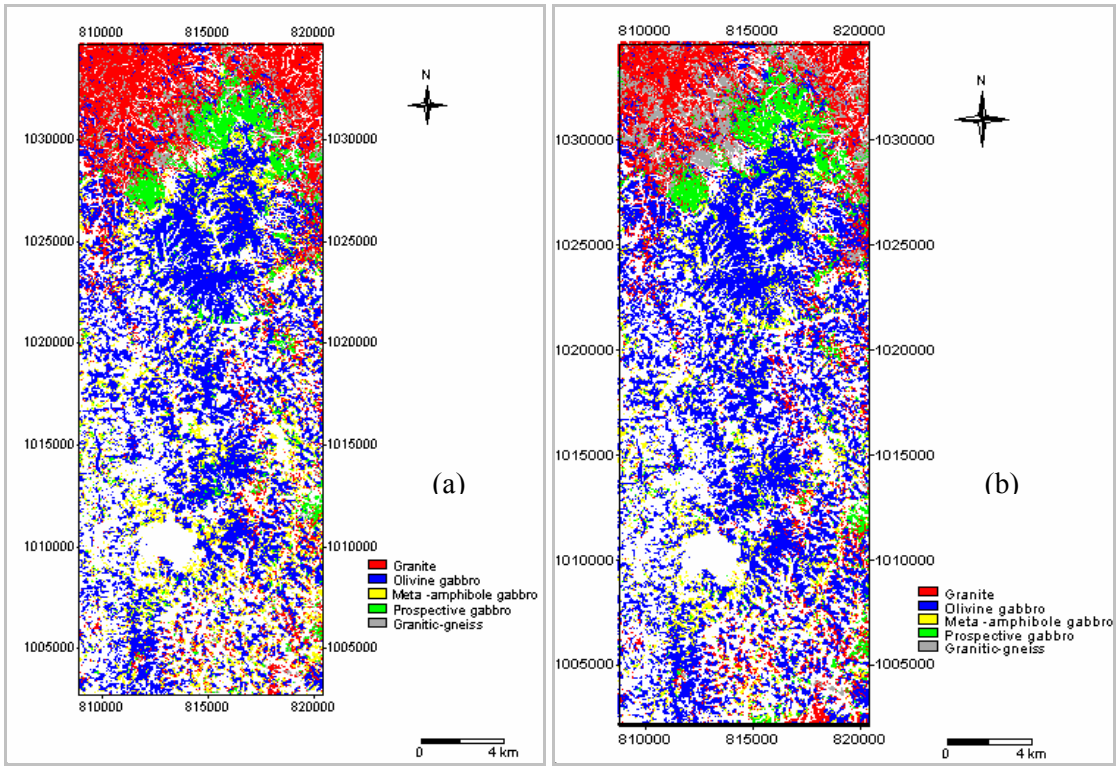

Figure 3.18: Classified images by MLC using input bands (a) TM 7/2-TM5/2-TM3/1 and (b) TM7/2-TM5/1-TM3/1.

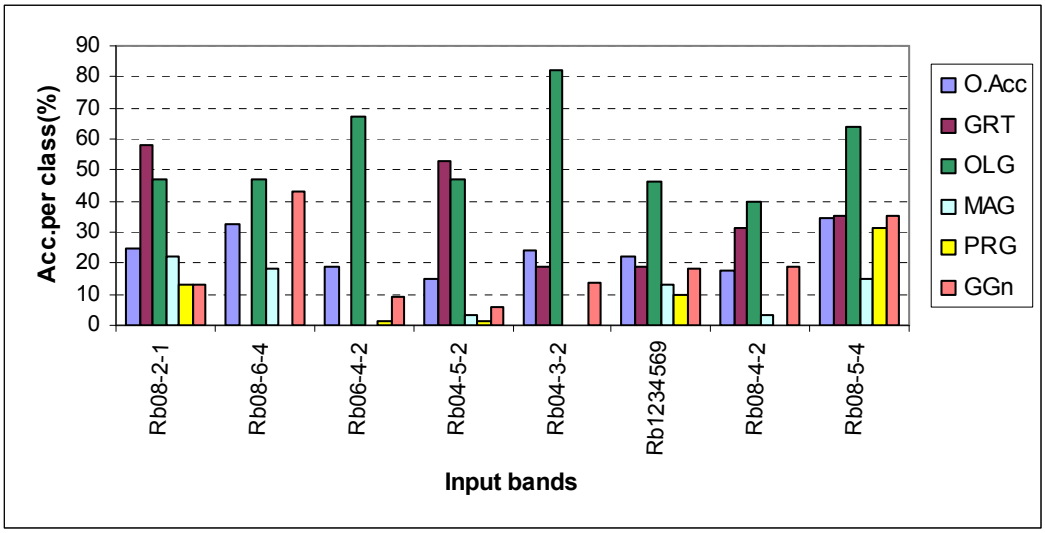

Figure 3.19: Classification accuracy (%) for each lithology class by using ASTER bands in MLC. (O.Acc = overall accuracy, GRT = granite, OLG = olivine gabbro, MAG = meta-amphibole gabbro, PRG = prospective gabbro and GGn = granitic-gneiss).

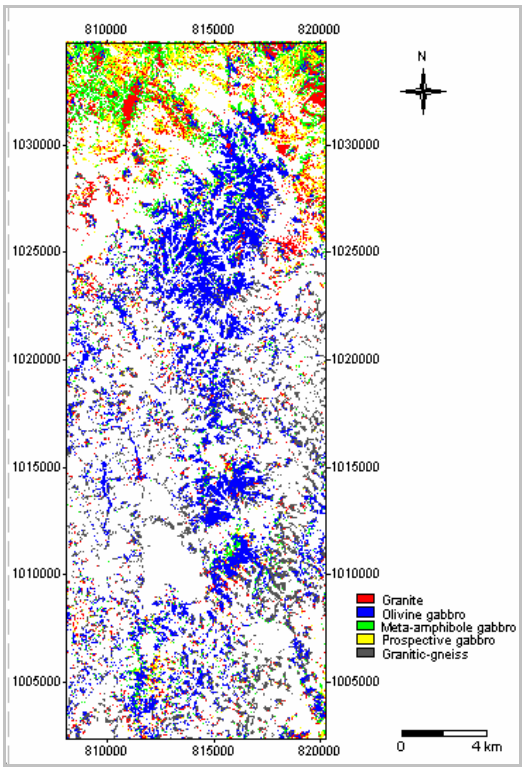

Figure 3.20: Classified image by MLC using ASTER bands Rb08, Rb05 & Rb04

3.5.2.2. Image classification using ASTER band ratios

Different band ratios of the ASTER data were used as inputs to MLC in order to create a thematic map. However, the overall classification accuracy of all combinations of input band ratios was below 30%. The classification accuracy (Figure 3.21) for granite (GRT) is more than 90% and for olivine gabbro (OLG) is more than 60%. The prospective gabbro (PRG) has very low classification accuracy of less than 20%. In general, the granite and the olivine gabbro are more enhanced than other units using band ratios as inputs to MLC.

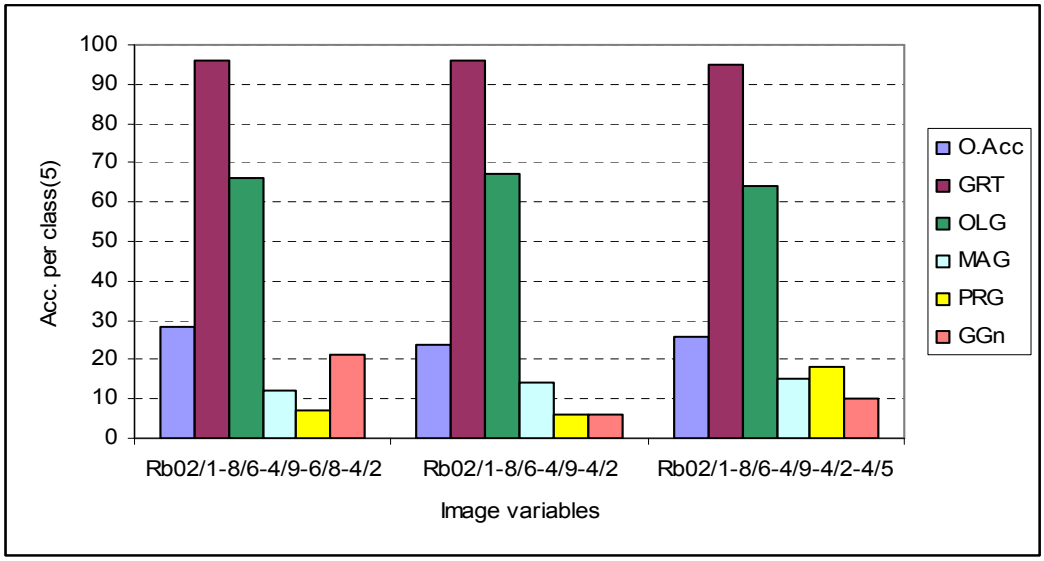

Figure 3.21: Classification accuracy (%) for each lithology class using ASTER band ratios in MLC. (O.Acc = overall accuracy, GRT = granite, OLG = olivine gabbro, MAG = meta-amphibole gabbro, PRG = prospective gabbro and GGn = granitic-gneiss)

The classified image created from input band ratios Rb02/Rb01, Rb04/Rb09, Rb04/Rb02, Rb08/Rb06 and Rb04/Rb05 (Figure 3.22) show limited spatial patterns of prospective gabbro in the northern parts of the area. This classified image has overall and average classification accuracy of 25.60% and 40.63%, respectively.

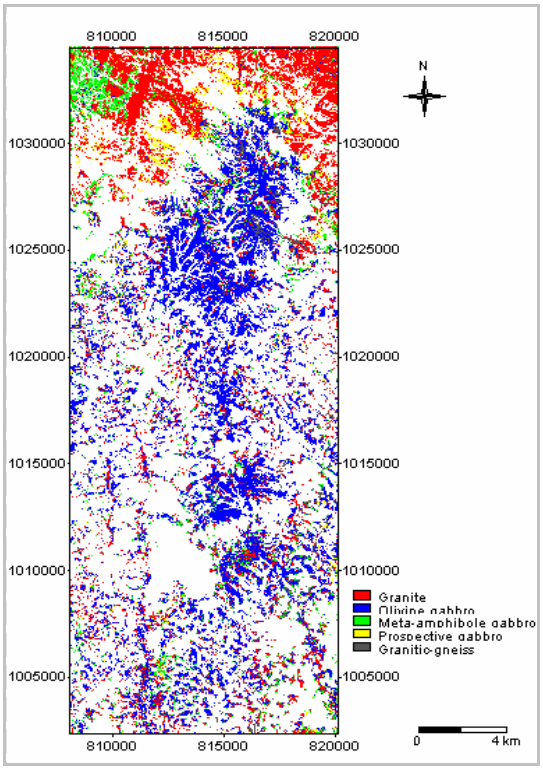

Figure 3.22: Classified image by MLC using input ASTER band ratios (Rb02/1, Rb04/9, Rb04/2, Rb08/6, Rb04/5)

3.6. Discussion and conclusion

3.6.1. Discussion

Landsat TM and ASTER satellite images having different sensor domains and with variable and broad spectral ranges can aid in mapping surficial geological features based on the diagnostic spectral features of minerals/rocks. Available multi-spectral data sets of Landsat TM and ASTER were tested to map lithology and mineralized zone in the study area.

The multi-spectral lithological remote sensing in this study includes PIMA analysis of rock samples, statistical descriptive analysis of DN-values of the lithologies in each band, and image transformation techniques (PCA and ratioing). All these procedures helped to select bands and band ratios that can be useful to discriminate the major lithologic units and prospective target area and these suitable bands were used in supervised classification methods in order to create a thematic map from image data.

Discriminating of major units and identifying the target area (prospective gabbro) from the background was possible through PCA as shown in image combination of TM PC3-4-5 and ASTER PC3-6-5 since they can express hidden information and relations between data sets. The PCA showed which bands that can show clay and iron variations as well as their overlaps in the study area.

The band ratio color composite image of Red=TM7/2, Green=TM5/2 (or TM5/1) and Blue=TM3/TM1 and band ratios Rb02/Rb01, Rb04/Rb09, Rb04/Rb02, Rb04/Rb05 and Rb08/Rb06, from ASTER, were found to be useful in enhancing the main rock groups as well as the prospective gabbro from the background since band ratios are less correlated than the original bands and enhance the mineralogical composition information in multi-spectral data.

The bands and band ratios of Landsat TM that were used as inputs to maximum likelihood classification were found to be better in identifying the prospective gabbro as compared to the ASTER bands. The better results obtained from the Landsat TM data rather than from ASTER data is probably due to the fact that the former data sets were acquired during relatively drier months (see section 2.5.1).

Supervised classification with five classes was tested using the suitable bands to map the major lithologic units in the study area. Using the confusion matrix, each image classification was tested and their results were compared to the published geological map as ground truth map. The confusion matrix identified the nature of the classification errors, as well as their quantities and the results of the confusion matrix highly depend on the selection of test set pixels. The overall accuracy for all image data used was less than 35%, which is very low. The poor results are probably due to vegetation and soil cover, scarcity of outcrops, nearly similar spectral response of rocks, landforms of the area that can affect the spectral property and the reliability of the published geological map.

However, the applied methods were useful in selection of optimal bands that can be useful in spectral pattern recognition of geological features in relatively dense vegetation area for mapping not only the major lithologic units of the area but also identifying of known mineralized zone.

3.6.2. Conclusion

- The methods used in this study based on PIMA analysis, spectral-lithology study based on statistical descriptive analysis, and image transformation (PCA and ratioing) assisted greatly in selecting the best bands and band ratios for lithologic remote sensing in the study area. The best bands and band ratios selected were useful not only in mapping major lithologies in the area but also suggest presence of clay, iron and their overlap zones in the geological set up of the area.
- In general, however, there is discrepancy between the ground truth map and the image units mainly in terms of contacts of units found in the northern part of the area.
- The overall accuracy of the lithologic classification based on single bands or band ratios is low, which can be due to some factors: presence of dense vegetation cover that hide the spectral contrast, similarity in mineral composition between rock units that implies similarity in spectral response, scarcity of outcrops, landforms of the area that can affect the spectral property and the reliability of the published geological map.

Chapter 4: Spatial Data Integration Modeling

This chapter has four objectives. The first objective is to integrate multi-spectral bands of Landsat TM data set, which were found to be more useful than the ASTER data set in lithologic mapping in the study area as shown in the previous chapter, with ancillary spatial data. The concept behind this first objective is to further enhance lithologic information by integration of multi-sensor data in order to create a new lithological map. The second objective is to apply the Spectral Angle Mapper (SAM) method to Landsat TM data in order to map minerals related to known apatite-mineralized zones in the study area. The idea behind this objective is to create images of minerals of interest that could be used to validate the newly created lithologic map, especially the interpretation of prospective gabbro units. The third objective is to create a predictive model of apatite-mineralized zones using old lithologic map and known apatite-mineralized zones in the study area. The idea behind this third objective is to cross-validate remotely-sensed prospective gabbro units and SAM-derived apatite image against predictive model of apatite-mineralized zones. The fourth objective is to integrate geo-information from remote sensing and predictive modeling to create an optimized map of promising targets for further exploration of apatite deposits.

4.1. Integration of multi-sensor data for lithological mapping

The objective of integrating data of different sensors is to further enhance information of interest (Christine Pohl, 1996) [9], (Nguyen Dinh Duong, 2002) [15]. In the previous chapter, it was found that some bands of Landsat TM data are useful in providing spectral information that allows mapping of the different lithologic units in the study area, although with poor accuracy. From the different derivative images from Landsat TM and/or ASTER data shown in the previous chapter (see for example Figure 3.12), there are noticeable differences in surface morphology and roughness of areas underlain by different lithologic units. In addition, the clear differences between mineralogical compositions of granitic rocks and gabbroic rocks suggest that each type of rocks have different resistance to weathering and therefore, produce different topographic features. Topographic data can be integrated with other spectral data for perspective visualization of unknown terrain, introduction of relief displacement into remotely sensed image to give stereo-optic viewing potential and the correction of remotely sensed data for variable solar illumination, (S.A. Drury, 1993) [16]. For this reason, topographic data are integrated or fused with the multi-spectral bands of Landsat TM data that were found useful in the previous chapter. The topographic data used here are in the form of a digital elevation model (DEM) derived from the same ASTER data sets used in the previous chapter.

4.1.1. Fusion of Landsat TM bands and ASTER DEM

To integrate multi-sensor images, remote sensing techniques such as pre-processing, adjusting to common coordinate system, geocoding to common georeference in order to have the same pixel position, fusing and visualization were applied, (Figure 4.1).

In order to integrate information of spectral features from Landsat TM and texture/pattern features from DEM image, the Brovey Transform image fusion, which is a simple technique to merge data from different sensors (E. Saroglu, et al.) [35], (Christine Pohl, 1996) [9] was applied. Generally, the Brovey Transform normalize the TM bands for RGB display and multiplies the result by other data to add the intensity or brightness component to the image, (Christine Pohl, 1996), [9]. The main steps used to form the fusion images were:

- Selection of bands and band ratios from Landsat TM that found useful in chapter 3 to discriminate the lithologic units of the area (in this case TM7, TM3, TM1 and band ratios TM7/2, TM5/1, TM3/1).
- Creating of combined intensity (CI) of the selected TM bands (in case of single bands as CI= TM7+TM3+TM1).
- Normalizing of each TM band as TM7/CI, TM3/CI, TM1/CI
- Creating of RGB image: Red= (TM7/CI)*DEM; Green= (TM3/CI)*DEM; Blue= (TM1/CI)*DEM.

- The same procedures were applied for band ratios TM7/2, TM5/1, TM3/1.

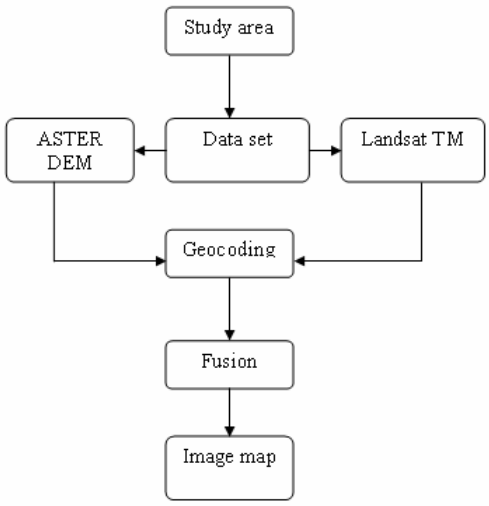

Figure 4.1: Flowchart of methodology for Landsat TM and DEM image fusion

4.1.2. Lithologic interpretation of fused image

To discriminate the different lithologic units found in the study area, the Landsat TM bands and band ratios were merged with ASTER DEM image. The fused images are in the form of a color composite (RGB) for visualization and interpretation as shown in Figure 4.2. The key elements applied to lithologic interpretation of the fused images are spectral patterns (in terms of color combination) and terrain features such as drainage pattern and density. These key elements for lithological analysis were applied simultaneously or interactively to the two fused images. The published geological map (Figure 2.2) was also consulted during lithologic interpretation of the fused images. The lithologic map based on interpretation of the fused images is shown in Figure 4.3.

4.1.3. Comparison of lithologic maps

As a result of fusing of multi-sensor data, different lithologic units are enhanced. For example, the fused image TM7-3-1 (RGB) can show differences of spectral features denoted by the dominance of OH-Fe minerals/rocks as reddish, Fe-bearing rocks denoted by greenish pixels and at the same time, surface roughness (for example areas mapped as meta-amphibole gabbro in the central and northern part) are different. The elliptical to irregular shape of body mapped as olivine gabbro shows smooth surface and the intrusion relationship of olivine gabbro with its surroundings is represented by lenticular shape with N-S trend appearing in the central to southern part of the area. Clear lithologic contacts marked by sharp color boundaries are enhanced in the northern part of the study area. Similarly, the fused band ratio image TM7/2-5/1-3/1(RGB), also show areas of iron-oxide bearing rocks in blue pixels and areas covered by hydroxylated minerals/rocks in reddish pixels and the overlap of TM7/2 and TM5/1 in yellowish pixels with the same terrain features as mentioned earlier. In the fused images, peculiar spectral signatures are apparent in areas mapped as prospective gabbro in the northern part of the study area and some small pixels with similar spectral signatures are also present within areas mapped as granitic-gneiss in the SE part of the study area. The areas mapped as granitic-gneiss are indicated to be composed of two sub-units based on the differences in spectral-terrain features. So combination of these interpreting elements was used to enhance the information and to interpret the different image units of the study area. Using such technique helps for human perception, improves the reliability and capability, and finally to discriminate the lithological boundaries and to highlight the subtle structures that unobserved by optical data (Christine Pohl, 1996), [9].

The new lithologic map is compared quantitatively with the published lithological map by crossing (or overlaying) these maps to create a confusion matrix (Table 4.1) and the results were interpreted as follows. The overall classification accuracy is about 68% [i.e., (418+55602+135844+10495+107724)/(456710)*100]. The classification accuracy for granite, olivine gabbro, meta-amphibole gabbro, prospective gabbro and granitic-gneiss is 20%, 73%, 78%, 52% and 59%, respectively. The results are better than in the previous chapter.

Table 4-1: Confusion matrix result for new geological map versus published geological map. (Values are number of pixels)

		Published lithologic map					
		Granite	Olivine gabbro	Meta-amphibole gabbro	Prospective gabbro	Granitic-gneiss	Total
New lithologic map	Granite	418				844	1262
	Olivine gabbro		55602	26758	4729	16825	103914
	Meta-amphibole gabbro (A & B)	1262	10728	135844	4704	50176	202714
	Prospective gabbro	403	10091	7999	10495	8548	37536
	Granitic-gneiss (A & B)			3281	279	107724	111284
	Total	2083	76421	173882	20207	184117	456710
	Classification accuracy (%) of interpreted lithologic unit	20	73	78	52	59	

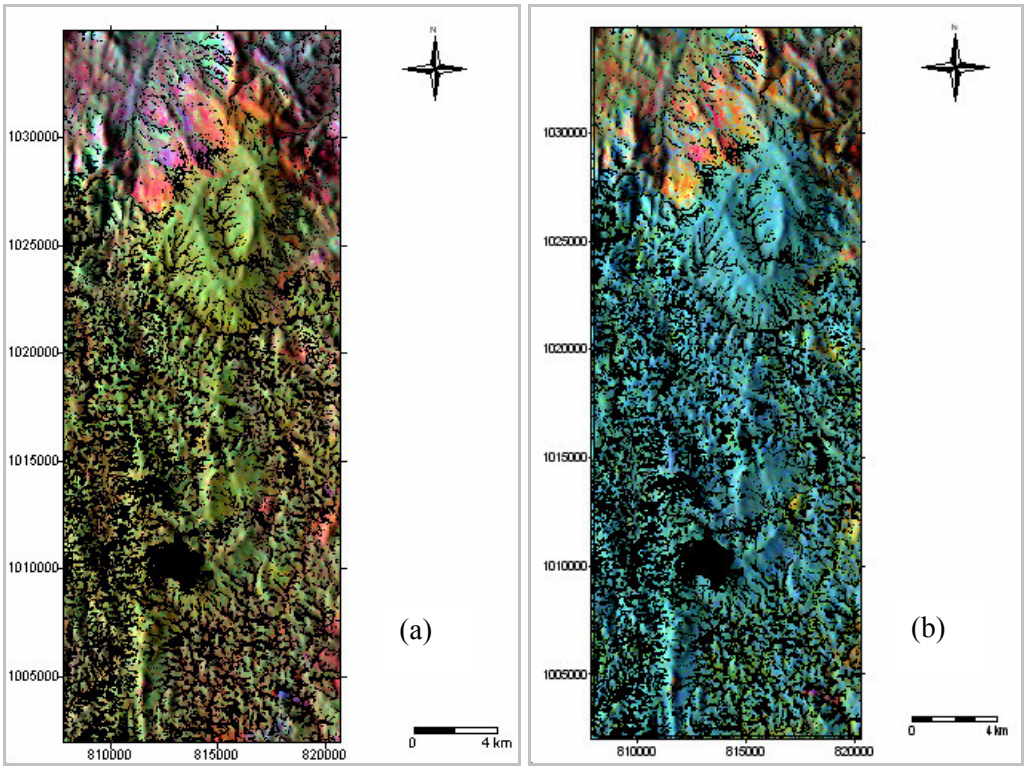

Figure 4.2: Color composite images based on (a) fusion of TM7-TM3-TM1 and ASTER DEM and (b) fusion of TM7/2-TM5/1-TM3/1 and ASTER DEM

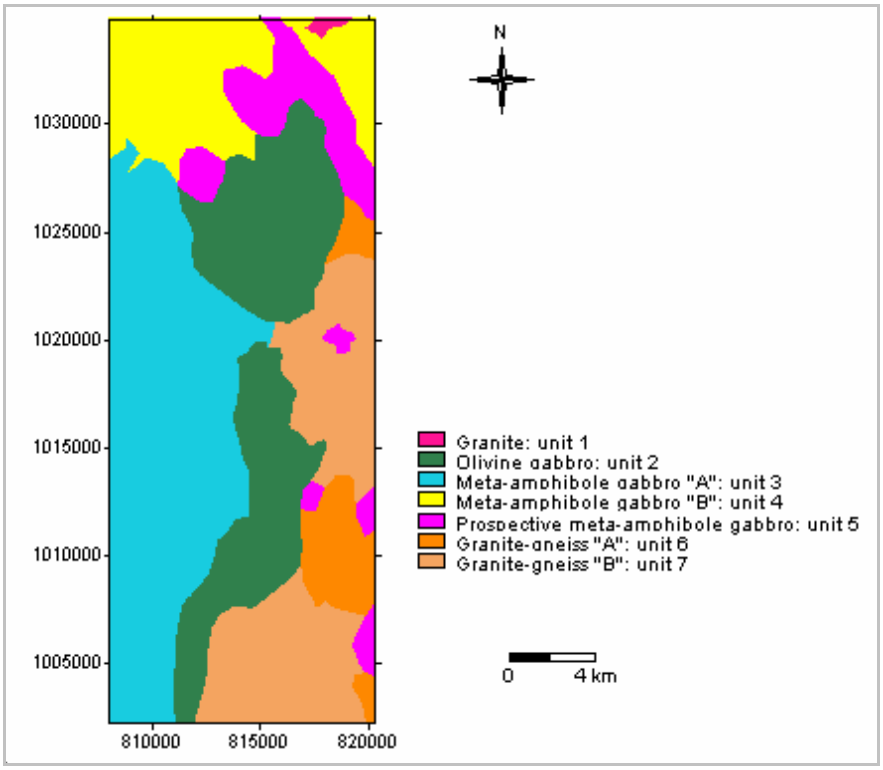

Figure 4.3: The integrated and generalized remote sensing geological map of the study area

4.1.4. Validation of interpreted of prospective gabbro unit

A binary map of apatite-mineralized zones was created from the geologic map (Figure 2.2). A binary map of interpreted prospective meta-amphibole gabbro was also created from new geological map (Figure 4.3). The two binary maps were then crossed (or overlaid) to obtain a confusion matrix, shown in Table 4.2, from which to estimate prediction rate of interpreted prospective gabbro in terms of delineating apatite mineralization in the study area.

Table 4-2: Cross table for binary maps of interpreted prospective gabbro and apatite-mineralized zones. (Values are number of pixels)

		Binary map of mineralized zone		
		Mineralized	Barren	Total
Binary map of interpreted prospective gabbro	Prospective gabbro present	10495	27041	37536
	Prospective gabbro absent	9712	409462	419174
	Total	20207	436503	456710

The overall accuracy of the interpreted prospective gabbro (in terms of prospective gabbro being present and absent) with respect to mapped prospective gabbro is 91.9% [i.e., (10495+409462)/(456710)*100]. The classification accuracy of interpreted prospective gabbro with respect to mapped prospective gabbro is 51.9% [i.e., (10495/20207)*100]. These all mean that prediction rate of interpreted prospective gabbro lies within the range of 51.9-91.9%, which indicates some degree of uncertainty for mineral exploration purposes. The high overall accuracy of the binary map of interpreted prospective gabbro is mainly due to the large area mapped as non-mineralized zone. The low classification accuracy of interpreted prospective gabbro could be due to presence of undiscovered apatite deposits in the study area and thus not indicated in the reference map. The validity of this latter hypothesis will be explored later (in sub-section 4.3.5) in this chapter.

4.2. Surficial Mineral Mapping

The objective of this section is to create surficial mineral map by comparing spectral data in Landsat TM band with reference spectrum using Spectral Angle Mapper (SAM) method. The most

common minerals found in the known mineralized zones in the study area are apatite, ilmenite, magnetite and hornblende. The last mineral (hornblende) is the main constituent of the host rock of the mineralization made up of the first three minerals. Reference spectrum for each of these four minerals was selected from the USGS mineral spectral library.

4.2.1. Spectral Angle Mapper (SAM) method

The Spectral Angle Mapper (SAM) calculates the spectral similarity between a test reflectance spectrum and a reference spectrum assuming the data are correctly calibrated to apparent reflectance with dark current and path radiance removed. The spectral similarity between the test spectrum and the reference spectrum is expressed in terms of the average angle between the two spectra (F. van der Meer, et al., 1997) [22]. The SAM algorithm maps spectral similarity using the arccosine of the dot products of image and reference spectra as vectors in n-dimensional space (where n is the number of bands) and computes the spectral angle between them. The SAM formula is defined as:

$$cos^{-1}\left[\frac{\sum_{b=1}^{n} i_b r_b}{\sqrt{\sum_{b=1}^{n} i_b^2 \sum_{b=1}^{n} r_b^r}}\right]$$

where, r represents amplitude of the reference spectrum at band b, and i represents amplitude of the test spectrum to be matched at band b.

The SAM classification is used because it is insensitive to gain factors (topography). It enables the user to compare image spectra with library spectra in a fast and interactive way that allows the user to easily adjust the lower and upper boundaries for a class and enables the user to work with training areas if there are no library spectra available.

4.2.2. The application of SAM method on Landsat TM data

A mini-library was created for reference spectra derived from the USGS mineral spectral library for known economic minerals (flour-apatite, hydroxyl-apatite, ilmenite, and magnetite) and gangue mineral (hornblende) in the study area. It was tried to compare these with Landsat TM image spectra using SAM method to create surficial mineral map of the study area. The classification threshold minimum values used for flour-apatite, hornblende, ilmenite, magnetite and hydroxyl-apatite were 0.45, 0.18, 0.46, 0.51 and 0.27, respectively. The result of the SAM classification is shown in Figure 4.4. The presence of economic minerals (mainly hydroxyl-apatite and ilmenite) is indicated to be mainly in the northern parts of the area. The distribution of hydroxyl-apatite more or less coincides with the known prospective gabbro (see Figure 2.2). Hornblende is also indicated to be present mostly in the northern parts of the area. Ilmenite is indicated to be interspersed in areas rich in hornblende. These areas rich in ilmenite and hornblende coincide with areas interpreted to be underlain by meta-amphibole gabbro “B” (see Figure 4.3). The mineral map, therefore, indicates differences in composition of meta-amphibole gabbros in the northern part and in other parts of the area. The mineral map (in terms of hornblende and ilmenite) validates interpretation of two units of meta-amphibole gabbro based on the fused images. However, the classified hydroxyl apatite pixels will be validated against known apatite-mineralized zones to quantify the accuracy of mineral map.

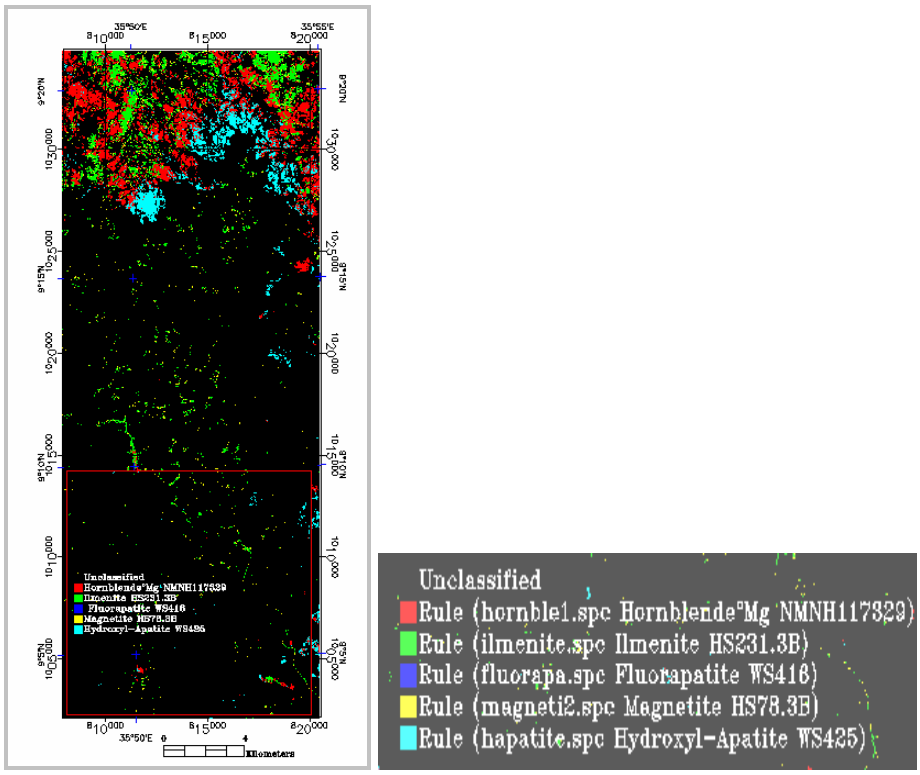

Figure 4.4: Surficial mineral map by SAM classification of Landsat TM bands

4.2.3. Validation

A binary map of apatite-mineralized zones and apatite-barren was created from the geologic map (Figure 2.2). A binary map indicating presence-absence of hydroxyl-apatite was also created from the SAM-classified mineral map. The two binary maps were then crossed (or overlaid) to obtain a confusion matrix, shown in Table 4.3, from which to determine prediction rate of SAM-classified hydroxyl-apatite in terms of delineating apatite mineralization in the area.

The overall accuracy of the mineral map (in terms of apatite being present or absent) is 94.8% [i.e., (3170+429739)/(456710)*100]. The classification accuracy of mapped hydroxyl-apatite with respect to known mineralized zone is 15.7% [i.e., (3170/20207)*100]. These all mean that prediction rate of SAM-classified hydroxyl-apatite lies within the range of 15.7-94.8%, which indicates high degree of uncertainty for mineral exploration purposes. The high overall accuracy of the binary hydroxyl-apatite map is mainly due to the large area where apatite mineralization has not been mapped in the field. The low classification accuracy of mapped hydroxyl-apatite could be due to (a) presence of vegetation and/or soil cover, which inhibits remote detection of bedrock mineralogy, or (b) presence of undiscovered apatite deposits, which are thus not indicated in the reference map. The validity of this latter hypothesis will be explored later (in sub-section 4.3.5) in this chapter.

Table 4-3: Cross table for binary maps of SAM-classified hydroxyl-apatite and apatite-mineralized zones. (Values are number of pixels)

		Binary map of mineralized zone		
		Mineralized	Barren	Total
Binary map of hydroxyl-apatite	Hydroxyl-apatite present	3170	6764	9934
	Hydroxyl-apatite absent	17037	429739	446776
	Total	20207	436503	456710

4.3. Predictive mapping of potential for apatite mineralization

The objective of this section is to create a predictive map of apatite-mineralization zones in the study area, and to compare the predictive mineralized zones with the interpreted prospective gabbro

(Figure 4.3) and the mapped hydroxyl-apatite (Figure 4.4). The predictive map is created based on published geological map. Because this published geological map can be considered imprecise (or having high degree of uncertainty), based on noticeable discrepancy when compared to the images derived from bands of Landsat TM and/or ASTER data, the predictive modeling is performed by application of Evidential Belief Functions (EBFs). The EBFs are considered to be adequate for representation and management of uncertainty in exploration data (An et al., 1994) [3].

4.3.1. Evidential Belief Functions method and its Implication

The Dempster-Shafer theory of evidence provides framework for estimation of EBFs (Dempster, 1967) [13]; Shafer, 1976) [36], which are integrated according to Dempster's (1968) [14] rule of combination. The following discussion for the application of EBF in this research is simplified and informal, because the theoretical formalization of EBFs is very involved.

Estimation of EBFs for spatial data is always in relation to a proposition, which in this case study is: "This location contains apatite deposits based on given spatial evidence". The EBFs are *Bel* (degree of belief), *Dis* (degree of disbelief), *Unc* (degree of uncertainty) and *Pls* (degree of plausibility) (Figure 4.5). *Bel* and *Pls* represent, respectively, lower and upper probabilities that evidence supports a proposition (Dempster, 1967) [13]. Thus, *Pls* is often greater than or sometimes equal to *Bel*. *Unc* is equal to *Pls–Bel* and represents ignorance (or doubt) of one's belief in the proposition based on a given evidence. If *Unc*=0, then *Bel*=*Pls*. *Dis* is belief that the proposition is false based on given evidence; it is equal to 1–*Pls* or 1–*Unc*–*Bel*. Thus, *Bel*+*Unc*+*Dis*=1. However, if *Bel*=0, then *Dis*=0 because there can be no disbelief if there is no belief; there can only be uncertainty. Interestingly, if *Unc*=0, then *Bel*+*Dis*=1, as in probability approach. The *Bel*, *Unc* and *Dis* are the EBFs used to integrate evidences according to Dempster's rule of combination (1968).

Procedures for data-driven estimation of EBFs proposed by Chung and Fabbri (1993) [10] and An, Moon and Bonham-Carter (1994) [3] are appropriate if locations of both mineralized and unmineralized zones are sufficiently known. In the case when locations of mineralized zones are fairly known but locations of "truly" unmineralized zones are insufficiently known, Carranza and Hale (2003) [8] proposed similar but different data-driven estimation procedures, which are adapted here and explained below.

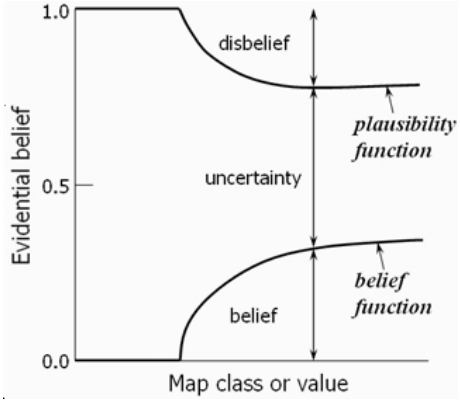

Figure 4.5: Schematic relationships of EBFs (modified after Wright and Bonham-Carter, 1996)

Suppose an exploration area T consists of $N(T)$ total number of unit cells or pixels and mineral deposits D occur in $N(D)$ number of pixels. Suppose further that spatial evidence maps X_i (i=1,2,…,n), with C_{ij} (j=1,2,…,m) classes of attributes, have been created for certain recognition criteria. By overlaying binary map of D on each evidential map, number of C_{ij} pixels overlapping with pixels containing D [i.e., $N(C_{ij} \cap D)$] and number of C_{ij} pixels not overlapping with pixels containing D [i.e., $N(C_{ij})-N(C_{ij} \cap D)$] are determined. The EBFs can then be estimated as follows.

$$Bel_{C_{ij}} = \frac{W_{C_{ij}D}}{\sum_{j=1}^{m} W_{C_{ij}D}} \quad (1)$$

where $W_{C_{ij}D} = \frac{\frac{N(C_{ij} \cap D)}{N(C_{ij})}}{\frac{N(D) - N(C_{ij} \cap D)}{N(T) - N(C_{ij})}}$.

The numerator to estimate parameter $W_{C_{ij}D}$ is conditional probability that *D* exists given presence of C_{ij}, which means that *D* occurs more (or is more present) in C_{ij} than would be expected due to chance. The denominator to estimate parameter $W_{C_{ij}D}$ is conditional probability that *D* exists given absence of C_{ij}, which means that *D* occurs more outside (or is more absent in) C_{ij} than would be expected due to chance. The parameter $W_{C_{ij}D}$ is, therefore, weight of C_{ij} in terms of *D* being more present than absent as may be expected due to chance. Thus, the degree of belief for C_{ij}, $Bel_{C_{ij}}$, as defined in Equation 1, is relative strength of $W_{C_{ij}D}$ for every j^{th} C_{ij} class of evidence in map X_i.

$$Dis_{C_{ij}} = \frac{W_{C_{ij}\overline{D}}}{\sum_{j=1}^{m} W_{C_{ij}\overline{D}}} \quad (2)$$

where $W_{C_{ij}\overline{D}} = \frac{\frac{N(C_{ij}) - N(C_{ij} \cap D)}{N(C_{ij})}}{\frac{N(T) - N(D) - [N(C_{ij}) - N(C_{ij} \cap D)]}{N(T) - N(C_{ij})}}$.

The numerator to estimate parameter $W_{C_{ij}\overline{D}}$ is conditional probability that *D* does not exist given presence of C_{ij}, which means that *D* occurs less (or is more absent) in C_{ij} than would be expected due to chance. The denominator to estimate parameter $W_{C_{ij}\overline{D}}$ is conditional probability that *D* does not exist given absence of C_{ij}, which means that *D* occurs less outside (or is more present in) C_{ij} than would be expected due to chance. This means that parameter $W_{C_{ij}\overline{D}}$ is weight of C_{ij} in terms of *D* being more absent than present as may be expected due to chance. Thus, the degree of disbelief for C_{ij}, $Dis_{C_{ij}}$, as defined in Equation 2, is relative strength of $W_{C_{ij}\overline{D}}$ for every j^{th} C_{ij} class of evidence in map X_i.

Equations 1 and 2 for data-driven estimation of *Bel* and *Dis*, respectively, were developed and demonstrated by Carranza and Hale (2003) [8] based on recommendations by (Chung and Fabbri , 1993)[10] to take into account not only (a) spatial relationship between an evidential map layer and target deposits but also (b) spatial relationships between classes of evidences in an evidential map layer. Note that, if for C_{ij} estimated $W_{C_{ij}D} = 0$, which means that $Bel_{C_{ij}} = 0$, then the corresponding estimated $W_{C_{ij}\overline{D}}$ should be re-set to zero, even if it is not, so that the corresponding $Dis_{C_{ij}} = 0$ according to Figure 4.5. *Unc* and *Pls* can then be estimated, respectively, as:

$$Unc_{C_{ij}} = 1 - Bel_{C_{ij}} - Dis_{C_{ij}} \quad (3)$$

$$Pls_{C_{ij}} = Bel_{C_{ij}} + Unc_{C_{ij}} \text{ or } Pls_{C_{ij}} = 1 - Dis_{C_{ij}} \quad (4)$$

Estimates of EBFs are usually held in attribute tables associated with spatial evidence maps X_i maps so that attribute maps of EBFs for X_i can be readily created. Maps of EBFs for X_1 can then be combined with maps of EBFs for X_2 according to Dempster's (1968) rule of combination in order to

generate an integrated map of EBFs. The formulas for combining maps of EBFs of two evidential maps (X_1 and X_2) are the following (adopted from Wright and Bonham-Carter, 1996) [39]:

$$Bel_{X_1X_2} = \frac{Bel_{X_1}Bel_{X_2} + Bel_{X_1}Unc_{X_2} + Bel_{X_2}Unc_{X_1}}{\beta} \quad (5)$$

$$Dis_{X_1X_2} = \frac{Dis_{X_1}Dis_{X_2} + Dis_{X_1}Unc_{X_2} + Dis_{X_2}Unc_{X_1}}{\beta} \quad (6)$$

$$Unc_{X_1X_2} = \frac{Unc_{X_1}Unc_{X2}}{\beta} \quad (7)$$

where $\beta = 1 - Bel_{X_1}Dis_{X_2} - Dis_{X_1}Bel_{X_2}$ is a normalizing factor to ensure that $Bel + Unc + Dis = 1$. $Pls_{X_1X_2}$ is estimated according to Equation 4. Only maps of EBFs of two spatial evidences can be combined each time; maps of EBFs representing $X_3, \ldots, X_n$ are combined one after another by repeated applications of Equations 5 to 7. Note however that the formulas for combining EBFs of two spatial evidences are commutative and associative, which means that different groups or orders of evidence combinations do not affect the final result. Final combination of maps of EBFs results in integrated *Bel*, *Dis*, *Unc* and *Pls* for the proposition based on given spatial evidences.

4.3.2. Deposit recognition criterion and spatial data sets

The known apatite deposits and associated Fe-Ti-oxide deposits are localized in zones within the meta-amphibole gabbro proximal to the contact with the olivine gabbro. The reason for this is that the deposits are probably associated with a basic magma that was fractionated from an olivine gabbro-rich composition to a hornblende-rich composition (EKIEP, 1988) [19], (Sisay A., 1992) [37]. In the study area, the mineralized zones occur near faults/lineaments (Figure 2.2) although it is unclear if these structures controlled the formation of apatite and Fe-Ti oxide deposits. However, similar deposits elsewhere are known to be associated with gabbro intrusive complexes deposited along deep-seated faults/fractures (Gross, 1995) [23]. In the field, as observed by the researcher during several exploration campaigns there, clay-rich and iron-oxide-rich soils characterize the overburden in the vicinity of the known apatite-magnetite-ilmenite deposits.

Based on the above discussion, the following three recognition criteria can be defined for predictive modeling of potential for apatite mineralization:

- Proximity of olivine gabbros;
- Proximity to faults/fractures; and
- Presence of clay-rich and lateritic soils.

The first recognition criterion is represented by first extracting the olivine gabbro unit from the published geological map, and then creating a map of distances around the olivine gabbro unit. The second recognition criterion is represented by a map of distance to faults/fractures. The faults/fractures used for predictive modeling were (a) digitized from the published geological map and (b) digitized from derivative images of Landsat TM band 4 after application of directional filters to enhance linear features (John A. Richards, 1993) [31]. The third recognition criterion is represented by a band ratio image of TM5/TM4, because both clay minerals and iron-oxide minerals generally have high reflectance in TM5 and low reflectance in TM4.

4.3.3. Estimation and integration of EBFs

The values in each of the maps used to represent the deposit recognition criteria were partitioned into a number of classes using 10-percentile intervals of the values. The classified deposit recognition criteria maps were then crossed with binary map of known mineralized zone, to obtain the parameters needed for the estimation of EBFs (see Equations 1 to 4) in section 4.3.1. The table below shows the estimated EBFs for the classes of values in the maps representing the deposit recognition criteria.

Most of the pixels in the known mineralized zone occur between 0.3-2.3 km away from the mapped olivine gabbro units. Therefore, the proximity classes of 290-1030 m, 1030-1675 m and 1675-2255 m have higher values of *Bel*, lower values of *Dis* and lower values of *Unc* as compared to the

other classes of proximity to olivine gabbro. These suggest that zones within 2.3 km from the olivine gabbro units could be prospective for apatite deposits, if the other recognition criteria are also present.

Most of the pixels in the known mineralized zone occur within 350 m of faults/fractures. Therefore, proximity classes up to 345 m have higher values of *Bel*, lower values of *Dis*, and lower values of *Unc* as compared to other classes of proximity to faults/fractures. These suggest that zones within 350 m of faults/fractures could be prospective for apatite deposits, if the other recognition criteria are also present.

A high proportion of pixels in the known mineralized zone occurs in areas with the highest class of TM5/TM4 ratio (2.945-23.5), therefore, the highest class of TM5/TM4 ratio has highest value of *Bel*, lowest value of *Dis*, and lowest value of *Unc* as compared to the other classes of TM5/TM4 ratio. These mean that areas with high TM5/TM4 ratio could be prospective to apatite deposits, if the other recognition criteria are also present.

Table 4-4: Estimates of EBFs for classes of values in maps of deposit recognition criteria for apatite mineral potential, Ghimbi-Bikilal

Proximity to olivine gabbro (m)	$N(C_{ij})$	$N(C_{ij} \cap D)$	*Bel*	*Dis*	*Unc*
0 (olivine gabbro unit)	76421	0	0.0000	0.0000	1.0000
1-290	15317	99	0.0349	0.1120	0.8531
290-1030	46022	1629	0.2448	0.1085	0.6467
1030-1675	45849	2701	0.5528	0.1056	0.3416
1675-2255	45947	1123	0.1504	0.1098	0.7398
2255-2830	46080	53	0.0057	0.1128	0.8815
2830-3465	46082	37	0.0040	0.1128	0.8832
3465-4200	45995	2	0.0002	0.1129	0.8869
4200-5215	45956	52	0.0056	0.1128	0.8816
5215-8730	46063	14	0.0015	0.1129	0.8856
Proximity to faults/fractures (m)	$N(C_{ij})$	$N(C_{ij} \cap D)$	*Bel*	*Dis*	*Unc*
0-60	44802	966	0.1773	0.0990	0.7237
60-120	42068	811	0.1546	0.0992	0.7462
120-190	45610	908	0.1614	0.0992	0.7394
190-260	45925	993	0.1784	0.0990	0.7226
260-345	49842	794	0.1249	0.0996	0.7755
345-430	41581	544	0.0996	0.0999	0.8005
430-550	48539	381	0.0570	0.1005	0.8425
550-695	46964	141	0.0209	0.1011	0.8780
695-925	44527	60	0.0093	0.1013	0.8894
925-2470	46852	112	0.0166	0.1012	0.8822
Alteration map (TM5/TM4)	$N(C_{ij})$	$N(C_{ij} \cap D)$	*Bel*	*Dis*	*Unc*
0-1.385	44836	189	0.0296	0.1009	0.8695
1.385-1.705	46684	516	0.0821	0.1001	0.8178
1.705-1.935	46293	729	0.1221	0.0996	0.7783
1.935-2.105	43853	605	0.1050	0.0998	0.7952
2.105-2.255	45674	489	0.0793	0.1002	0.8205
2.255-2.395	47728	394	0.0598	0.1005	0.8397
2.395-2.525	45322	324	0.0514	0.1006	0.8480
2.525-2.675	45876	309	0.0482	0.1006	0.8512
2.675-2.945	47104	466	0.0727	0.1003	0.8270
2.945-23.5	46362	1689	0.3498	0.0973	0.5529

In order to integrate the EBFs of the classes of values in maps representing the deposit recognition criteria, attribute maps of *Bel*, *Dis* and *Unc* for the three sets of evidential data were first created (Figures 4.6 to 4.8). Maps of integrated *Bel*, *Dis* and *Unc* were then derived by application of Equation 5 to 7. A map of integrated *Pls* was created by addition of maps of integrated *Bel* and *Unc* (Equation 4).

The mapped apatite-magnetite-ilmenite deposits were overlaid on the maps of integrated EBFs (Figure 4.9). Most of the known apatite occurrences lie on areas with high degrees of *Bel*, low degrees of *Dis*, low degrees of *Unc*, and high degrees of *Pls*. This indicates that the maps of integrated EBFs can indicate other zones with potential for apatite mineralization in the study area.

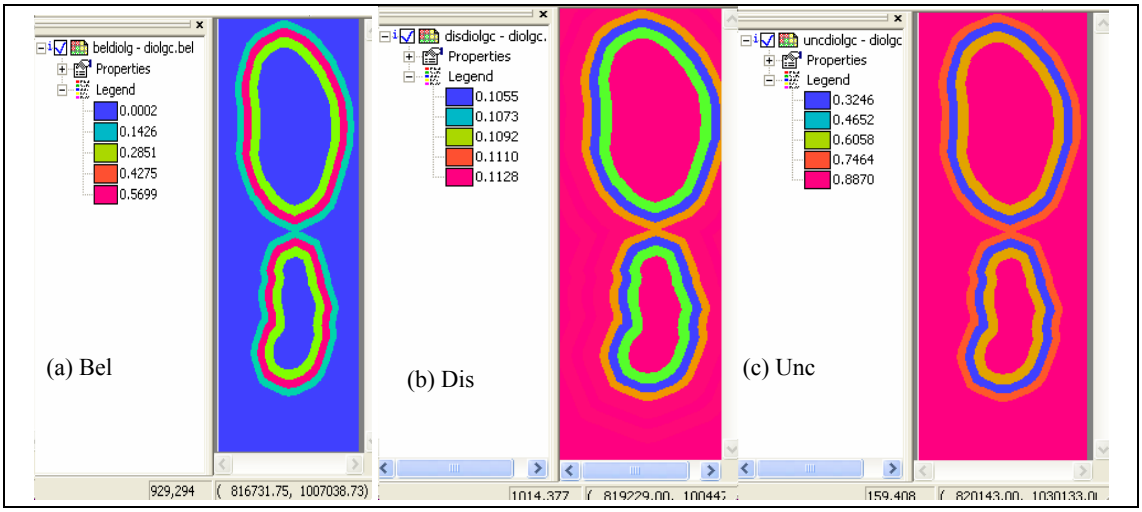

Figure 4.6: Maps of EBFs for classes of proximity to olivine gabbro with respect to known apatite-mineralized zone: (a) *Bel*, (b) *Dis*, (c) *Unc*.

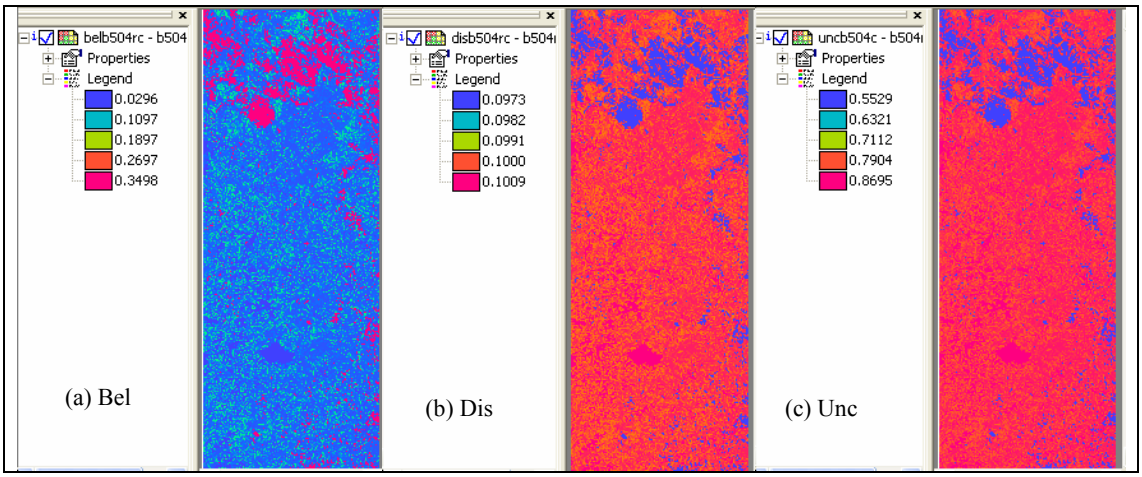

Figure 4.7: Maps of EBFs for classes of TM5/TM4 ratios (representing clay-rich and iron-oxide rich criteria) with respect to known mineralized zone: (a) *Bel*, (b) *Dis*, (c) *Unc*.

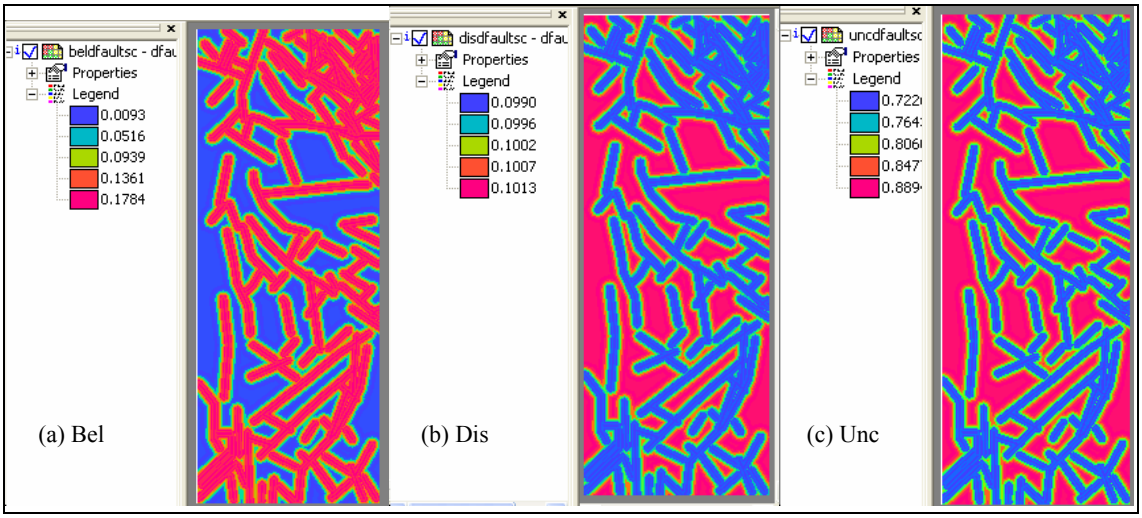

Figure 4.8: Maps of EBFs for classes of proximity to faults/fracture with respect to known apatite mineralized zone: (a) *Bel*, (b) *Dis*, (c) *Unc*

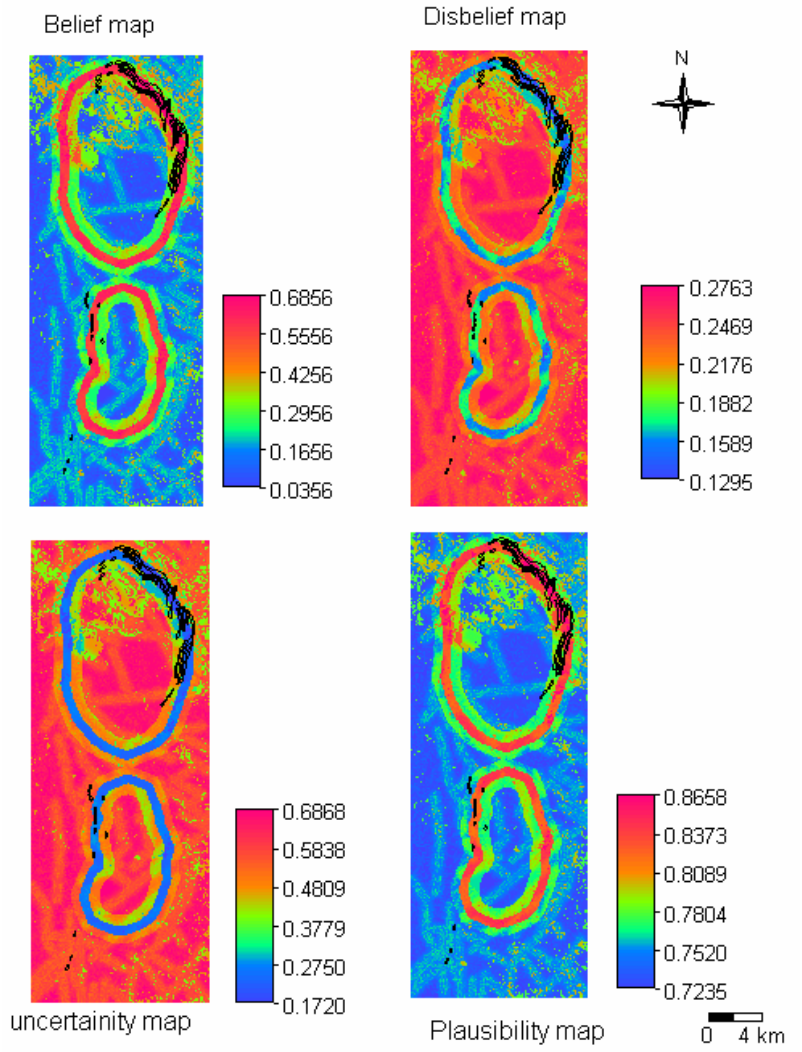

Figure 4.9: Maps of integrated *Bel*, *Dis*, *Unc* and *Pls*. Areas in black are known apatite-magnetite-ilmenite deposits

4.3.4. Classification and validation of potential apatite-mineralized zones

In order to map zones with potential for apatite deposits, the map of integrated *Bel* was used because high degrees of *Bel* relate directly to the known apatite occurrences. The map of integrated *Pls* can also be used for this purpose, but it includes degree of *Unc* (see equation 4). The map of integrated *Bel* was classified using values corresponding to 50, 75, 90 and 100 percentiles to map zones of different degrees of potential for apatite deposits. The different degrees of potential for apatite deposits are very low (0-50 percentile), low (50-75 percentile), moderate (75-90 percentile) and high (90-100 percentile). The classified map of potential for apatite deposits is shown in Figure 4.10.

The classified apatite potential map (Figure 4.10) was crossed with binary map of mineralized to estimate success rate of predictive modeling. From the resulting cross table (table 4.5), it can be observed that the sum of pixels of mineralized zone delineated in predicted moderate to high potential zones is 16658. This means that 82.4% of mapped mineralized zone pixels coincide with portions of predicted moderate to high potential zones. From table 4.5, it can be also observed that the sum of pixels of absent for mineralized zone predicted by very low to low potential zones is 338904. This means that 77.6% of mapped barren zone pixels coincide with portions of predicted very low to low potential zones. These all mean that success rate of predictive modeling lies in the range 77.6-82.4%, which (a) indicates a satisfactory fit between the evidential data and training target data (i.e., known mineralized zone) and (b) suggests usefulness of predictive apatite potential map for further

exploration of undiscovered apatite deposits. The latter needs further verification by estimation of prediction rate.

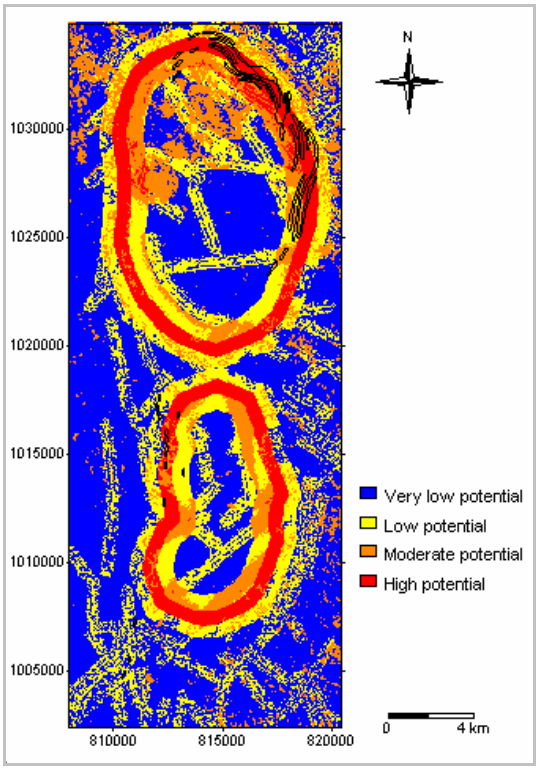

Figure 4.10: Predictive map of apatite deposit potential based on integrated *Bel*

Table 4-5: Cross table for predictive map of apatite potential and map of known apatite-mineralized zone. (Values are number of pixels)

Mineral potential classification	Binary map of mineralized zones		Total
	Mineralized	Barren	
Very low potential	183	227970	228153
Low potential	3366	110934	114300
Moderate potential	6946	61486	68432
High potential	9712	36113	45825
Total	20207	436503	456710

The classified apatite potential map (Figure 4.10) was also crossed with a binary map of known apatite-magnetite-ilmenite deposits (see Figure 2.2) in order to estimate prediction rate of classified apatite potential map. From the resulting cross table (table 4.6), it can be observed that the sum of pixels of known apatite-magnetite-ilmenite deposits present in predicted moderate to high potential zones is 4640. This means that 80.7% of known apatite-magnetite-ilmenite deposit pixels coincide with portion of predicted moderate to high potential zones. From table 4.6, it can be also observed that the sum of pixels representing absence of known apatite-magnetite-ilmenite deposit predicted by very low to low potential zones is 341383. This means that 75.7% of pixels representing absence of known apatite-magnetite-ilmenite deposits coincide with portions of predicted very low to low potential zones. These all mean that prediction rate of classified apatite potential map lies in the range 75.7-80.7%, which indicates (a) satisfactory prediction of potentially apatite-mineralized zones and (b) low degree of uncertainty of the predictive model for exploration purposes. The predictive apatite potential can therefore be useful for further exploration of undiscovered apatite deposits in the study area.

Table 4-6: Cross table for map of predictive apatite potential and map of known apatite-magnetite-ilmenite deposits. (Values are number of pixels)

Mineral potential classification	Binary map of apatite-magnetite-ilmenite deposits		Total
	Apatite-magnetite-ilmenite deposits present	Apatite-magnetite-ilmenite deposit absent	
Very low potential	154	227999	228153
Low potential	916	113384	114300
Moderate potential	1755	66677	68432
High potential	2885	42940	45825
Total	5710	451000	456710

Because of satisfactory success and prediction rates of classified apatite potential map, it can be used to further cross-validate the interpreted prospective gabbro (Figure 4.3) and the mapped of hydroxyl-apatite by SAM method (Figure 4.4).

4.3.5. Cross validation of remotely-sensed information with predictive model

The binary map of interpreted prospective gabbro, created from the new lithologic map (Figure 4.3), was crossed with the classified predictive map shown in Figure 4.10. From the resulting cross table shown in table 4.7, sum of pixels of interpreted prospective gabbro in predicted moderate to high potential zones is 22997. This means that at least 61.3% interpreted prospective gabbro pixels coincide with portions of predicted moderate to high potential zones. From table 4.7, the sum of pixels of interpreted non-prospective gabbro in predicted very low to low potential zones is 327914. This means that at least 78.2% interpreted non-prospective gabbro coincide with portions of predicted very low to low potential zones. These all mean that there is good agreement (61.3-78.2%) between the new lithologic map (in terms of interpreted prospective gabbro) and the predictive map of apatite potential. In addition, the cross-validation result suggests that interpreted prospective gabbro unit can be useful to guide further exploration for undiscovered apatite deposits in the study area.

Table 4-7: Cross table for map of predicted of apatite potential and map of interpreted prospective gabbro. (Values are number of pixels)

Classification	Prospective gabbro present	Prospective gabbro absent	Total
Very low potential	7429	220724	228153
Low potential	7110	107190	114300
Moderate potential	14933	53499	68432
High potential	8064	37761	45825
Total	37536	419174	456710

The binary map indicating presence-absence of hydroxyl-apatite, created from the SAM-classified mineral map (Figure 4.4), was also crossed with the classified predictive map shown in Figure 4.10. From the resulting cross table shown in table 4.8, the sum of pixels of mapped hydroxyl-apatite in predicted moderate to high potential zones is 9370. This means that at least 94.3% of mapped hydroxyl-apatite pixels coincide with portions of predicted moderate to high potential zones. From table 4.8, the sum of mapped non-hydroxyl-apatite pixels in predicted very low to low potential zones is 341889. This means that at least 76.5% of mapped non-hydroxyl-apatite pixels coincide with predicted very low to low potential zones. These all mean that there is good agreement (76-94%) between binary map of remotely-sensed hydroxyl-apatite and predictive map of apatite potential. In addition, the cross-validation result suggests that the SAM-classified pixels can be useful to guide further exploration for undiscovered apatite deposits in the study area.

Table 4-8: Cross table for map of predicted apatite potential and map of SAM-classified hydroxyl-apatite. (Values are number of pixels)

Classification	Hydroxyl-apatite present	Hydroxyl-apatite absent	Total
Very low potential	244	227909	228153
Low potential	320	113980	114300
Moderate potential	6441	61991	68432
High potential	2929	42896	45825
Total	9934	446776	456710

4.3.6. Optimization of a predictive map for promising exploration targets

Because high proportions of interpreted prospective gabbro and SAM-classified hydroxyl-apatite pixels coincide with predicted moderate to high potential zones, these three sets of geo-information can be integrated to derive an optimized predictive map of promising exploration targets for apatite deposits. The following steps were undertaken to derive an optimized predictive map of promising exploration targets for apatite deposits.

Classified predictive map of apatite potential (Figure 4.10) was further classified into a binary value map by assigning a score (S_b) of 1 to moderate to high potential zones and assigning a score (S_b) of 0 to low to very low potential zones. The other binary thematic maps were also converted to binary value maps. Map of unit of interpreted prospective gabbro was given a score (S_b) of 1, whereas other map units were given a score (S_b) of 0. Pixels of SAM-classified hydroxyl-apatite were given a score (S_b) of 1, whereas other SAM-classified pixels were given a score (S_b) of 0. Each of the three binary score (S_b) maps were then assigned weights (W_m) equal to average prediction rate of the corresponding maps from which the binary score maps were created. For the binary score (S_b) map of interpreted prospective gabbro, the weight (W_m) assigned is 0.719 (i.e., average of prediction rate range of 51.9-91.9%; see section 4.1.4). For the binary score (S_b) map of SAM-classified hydroxyl-apatite, the weight (W_m) assigned is 0.5525 (i.e., average of prediction rate range of 15.7-94.8%; see section 4.2.3). For the binary score (S_b) map of predicted apatite potential, the weight (W_m) assigned is 0.782 (i.e., average of prediction rate range of 75.7-80.7%; see section 4.3.4). The weighted binary score maps are integrated through a simple index overlay model, to derive exploration target scores (S_t), which range from 0 to 1, according to the following formula (after Bonham-Carter, 1994)[6]:

$$S_t = \frac{\sum (S_b \times W_m)}{\sum W_m} . \tag{8}$$

The output target score map was then classified as follows. Zones with S_t <0.333 were considered "poor" exploration targets. Zones with S_t of 0.333-0.666 were considered "good" exploration targets. Zones with S_t > 0.666 were considered "very good" exploration targets. Figure 4.11 shows the optimized predictive map of promising exploration targets for apatite deposits.

The prediction rate of the optimized predictive map of promising exploration targets was estimated by crossing it with the binary map of known apatite-magnetite ilmenite deposits. The resulting cross table is shown in Table 4.9. Considering map units classified as "good" and "very good" targets as one map unit, the overall classification accuracy of the optimized predictive map is 72.7% [i.e., (2386+2629+327219)/(456710)*100]. The classification accuracy of "good" and "very good" targets is 87.8% [i.e., (2386+2629)/(5710)*100]. The classification accuracy of "poor" targets is 72.6% [i.e., (327219)/(45100)*100]. The prediction rate of the optimized predictive map of promising exploration targets lies in the range of 72.6-87.8%, or probably an average prediction rate of 80.2%. Integration of the remotely-sensed information with the geo-information from the predictive modeling results in an optimized predictive map of promising exploration targets with an increased prediction rate, from an average of 78.2% to an average of 80.2%. Based on this good prediction rate, the optimized predictive map of promising exploration targets for apatite deposits could be used in guiding further exploration for apatite deposits in the study area. In particular, many portions of zones classified as "very good" targets that do not coincide with known apatite deposits warrant further field ground-truthing.

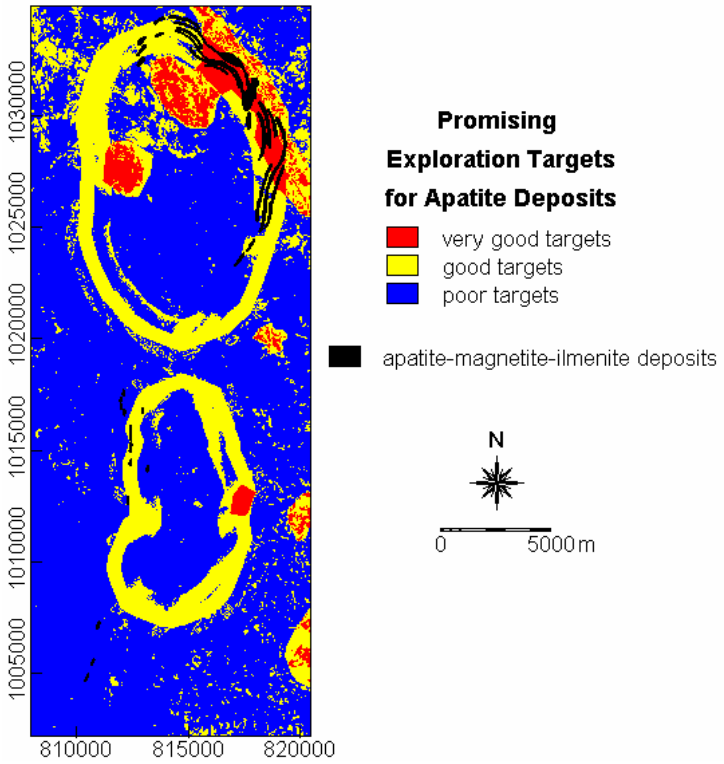

Figure 4.11: Optimized predictive map of promising exploration targets for apatite deposits

Table 4-9: Cross table for optimized predictive map of exploration targets and map of known apatite-magnetite-ilmenite deposits. (Values are number of pixels)

Classification	Apatite-magnetite-ilmenite deposits present	Apatite-magnetite-ilmenite deposit absent	Total
Poor targets	695	327219	327914
Good targets	2386	103413	105799
Very good targets	2629	20368	22997
Total	5710	451000	456710

4.4. Discussion and conclusion

4.4.1. Discussion

In the fused images as shown in Fig 4.2a & b, the BLGC of the area is expressed by variation in color (tone, texture) and terrain features (roughness, drainage density and pattern). The distinguishing features for unit2, which is mapped as olivine gabbro in the published geological map that covers the central and northern part of BLGC, are its shape and structural relationship with rocks, which it intrude is clearly observed. The olivine gabbro unit occurs as elliptical body with relatively smooth terrain and sub-parallel drainage patterns. Other units of the olivine gabbro intrusion are present in southern parts of the area as narrow and long vertical dyke-like bodies running in almost N-S direction. The area underlain by image unit3, is shown by rough (rugged) surface and dense drainage pattern, which is different from the northern part (unit4), which is mapped as the same unit as meta-amphibole gabbro as shown in the published geological map. Similarly, the unit7 and unit6, which were mapped as granitic-gneiss underlain in south, SE and eastern part of the area, showed different spectral signatures, surface roughness (rugged) and drainage patterns. The previously mapped areas of granitic-gneiss can be discriminated from the meta-amphibole gabbro and the olivine gabbro and can be divided into two sub-units based on the fused images.

The band ratio images TM7/2, TM5/1, TM3/1 fused with DEM image as shown in Figure 4.2b shows areas of alteration and mineralization associated with hydroxyl and iron variations. In general, fusing of multi-sensor satellite data sets is found to be useful in this study, because the various lithologic units including the prospective gabbro are fairly distinct from each other due to their spectral signatures and topographic features, which are together vital for lithologic mapping.

The selected common minerals used as reference in SAM classification method are generally distributed in the northern part of the study area and cover some part of the known prospective gabbro as indicated in the published geological map. The result of SAM classification indicates presence of hornblende and ilmenite in unit4 as shown in the interpreted geological map (Figure 4.3), whereas this unit was mapped mostly as granitic-gneiss as shown in the published geological map (Figure 2.2). The result of SAM classification also confirms presence hydroxyl-apatite, which consists with known type of apatite in the area (IFDC, 1987) [28]. But the interesting thing is the mineral map shows the occurrence of apatite with similar spatial pattern with prospective gabbro and areas enhanced well by band ratio combination TM7/2-TM5/1 (or TM5/2)-TM3/1 (RGB).

The application of evidential belief functions to mapping of apatite mineral potential in the study area showed importance of spatial evidences such as TM5/4 ratios (representing clay-rich and iron-rich soil), and proximity to olivine gabbro and to faults/fractures. The Dempster's rule of combination also helped to integrate the selected evidential data to create final evidential belief functions. Based on this, final belief, disbelief, uncertainty and plausibility maps were created for the study area. From the map of integrated Bel, predictive apatite deposit potential map was created. Finally, an optimized predictive map of promising exploration targets for apatite deposits was created from the combination of interpreted prospective gabbro, SAM-classified hydroxyl-apatite and predictive potential map.

4.4.2. Conclusion

- Merging data sets of spectral reflectance (characteristic of materials) and of topographic information served to enhance geological features and facilitates mapping of the lithologic units in the study area.
- ASTER DEM data was useful to enhance structural and terrain features that can assist in geological mapping. Information variation in texture and surface roughness are important in areas or objects having similar spectral characteristics.
- Using SAM method, the reference spectrum was compared with image spectrum and finally, the distributions of the most common minerals were identified. The importance of SAM methods here is twofold, one is in identifying the most economic minerals and secondly the possibility in discriminating lithologic units, which were mapped previously as one unit. This shows that the SAM method in Landsat TM data can be helpful in geological mapping and targeting potential areas for mineral exploration.
- The potential map created by EBFs was crossed with SAM-classified apatite occurrence map and interpreted prospective gabbro for validation. High proportions of the mapped apatite and interpreted prospective gabbro lie within the moderate to high potential classes of predictive map. Therefore, to derive an optimized predictive model, binary maps of interpreted prospective gabbro, SAM-classified hydroxyl-apatite and predictive potential map were integrated through a simple index overlay technique.
- Resulting optimized predictive map of promising exploration targets for apatite deposits has an estimated average prediction rate of 80.2%. It could be useful in guiding further exploration for apatite deposits in the study area.
- In general, the different methods applied in this study helped to extract, to compare and to integrate the geological information and finally to create a new geological map and an optimized predictive map of new exploration targets for apatite deposit in the study area.

Chapter 5: Overall Conclusions and Recommendations

5.1. Conclusions

- The application of remote sensing and spatial data integration modeling with optimal methods as applied in this study, were useful in lithologic mapping even though the area is characterized by less spectrally separable surficial geological features due to similarity in rock composition, presence of dense vegetation and soil cover.
- PIMA analysis, descriptive analysis of image data, and image transformation were altogether useful in selection of multi-spectral bands or band ratios that can be very useful in lithologic mapping in the study area.
- The overall accuracy of multi-spectral image classification for lithologic mapping is very low. This may be due to vegetation and soil cover, similarity in mineral composition of the lithologic units, landforms of the area that can affect the spectral property, scarcity of outcrops and reliability of the published geological map.
- Fusion of multi-spectral data with digital elevation data was useful in enhancing the different lithologic units in the study area. The method allowed creation of new lithological map.
- Satellite imagery data, processed by appropriate methods, as used here are useful not only in interpreting the geologic features, but also locating new information in addition to the previously known geologic features and identifying specific and important geologic features for economic minerals in the geological environment of the study area at reconnaissance scale.
- The use of SAM classification helped to confirm the presence of compositional difference in units previously mapped as one unit (in terms of the mineral distribution) and the occurrence of economic minerals. The economic minerals are spatially distributed almost with similar pattern with the known prospective zone of the northern part of the study area. This means that the SAM classification in Landsat TM can be helpful in geological mapping and targeting the potential areas for mineral exploration.
- The potential map created by EBFs, showed that the apatite deposits of the study area lie in moderate to high potential zones and these coincide with high proportions of interpreted prospective gabbro and SAM-classified apatite. Therefore, the combination of these three sets of spatial data information was considered useful to derive an optimized predictive map of promising exploration targets for apatite deposits.

5.2. Recommendations

- The result of this study showed the usefulness of remote sensing in geological mapping of BLGC and its associated mineralization, and it is recommended to implement it for mapping other gabbroic intrusion with associated Fe-Ti-P mineralization that occurs in similar geological setting in remote areas of poor accessibility.
- The optimized predictive map of promising exploration targets for apatite deposits can be used, with caution, to guide further exploration of apatite deposits in the test area.
- It is also recommended to use remote sensing data with high spectral and spatial resolutions to delineate the apatite-bearing units in more detail. In addition to this, using complementary geophysical data sets such as magnetics to discriminate mafic rocks as well as the iron deposit of Bikilal area, which is closely associated with the apatite deposits and radiometric data to discriminate the different type of granitoid rocks found in the study area may help to improve the result obtained in this research.

References

1. Michael J. Abrams, Imaging Spectrometry in the thermal infrared, chapter 10, Basic physics of spectrometry,
2. Amenti A. 1989, Tectonic history of the pan African low-grade belt of western, Ethiopia, pp16.
3. An, P., Moon, W.M., and Bonham-Carter, G.F., 1994, Uncertainty management in integration of exploration data using the belief functions: Nonrenewable Resources, v. 3, no. 1, p. 60-71.
4. Aussois (Modane), 1988, spectral Signatures of objects in Remote sensing, p337-340.
5. Berhe G.S., 2001, Geology and evaluation of apatite and magnetite-ilmenite Resources of Soji-Gerjo Bikilal area.
6. G.F. Bonham-Carter, 1994, Geographic Information System For Geoscientists modeling with GIS, p285-286
7. E.J.M. Carranza, 2002, Geologically-Constrained Mineral Potential Mapping, (examples from the Philippines), Ph.D. thesis, ITC publication Number 86
8. E.J.M. Carranza and M. Hale, 2003, Evidential belief functions for Data-driven geologically constrained mapping of Gold Potential, Baguio district, Philippines, ELSEVIER, Ore Geology Reviews 22(2002) 117-132
9. Christine Pohl,1996, Geometric Aspect of Multi-sensor image fusion for Topographic map Updating in the Humid Tropics, ITC publication no.39
10. Chung, C.F. and Fabbri, A., 1993, The representation of geoscience information for data integration: Nonrenewable Resources, v. 2, no. 2, p. 122-139.
11. Consult 4 International, 2002, Bikilal Phosphate Exploration and Pre-Feasibility Study, final report 273563, prepared for Geological Survey of Ethiopia.
12. Crosta, A.P. and Rabelo A., 1993, Assessing Landsat TM for hydrothermal alteration mapping in central-western Brazil. Proceedings of Ninth Thematic Conference on Geologic Remote Sensing, Pasadena, California, USA, 8-11,febraury 1993,pp.1053-1061.
13. Dempster, A.P., 1967, Upper and lower probabilities induced by a multivalued mapping: Annals of Mathematical Statistics, v. 38, p. 325-339.
14. Dempster, A.P., 1968, Generalization of Bayesian inference: Journal of the Royal Statistical Society, series B, v. 30, p. 205-247.
15. Nguyen Dinh Duong, Combination of multi-spectral and SAR remote sensing data for urban study, http://www.gisdevelopment.net/aars/acrs/2002/urb/085.pdf
16. S.A. Drury,1993, Image interpretation in Geology, second edition, chapter5, Digital image processing pp124-156
17. Eastman,1995, Image classification
18. Efrem B.,2001,The geology of Ghimbi-Bikilal area, GSE, Ethiopia
19. EKIEP, 1988, Exploration and Evaluation of Bikilal Iron Ore Deposit, Wollega, Ethiopia, phase II, EIGS note No.322, pp166.
20. Ernst M. Schetselaar, et al., 2000, Integration of Landsat TM, Gamma-Ray, Magnetic, and a Field Data to Discriminate Lithological Units in Vegetated Granite-Gneiss Terrain, Remote Sensing Environment 71:89-105 (2000)
21. F. van der Meer, July 25, 2002, ILWIS application 14, Remote Sensing and GIS Techniques applied to geological Survey, pp167-180
22. F. van der Meer, M. Vazquez-Torres and P.M. Van Dijk, 1997, Spectral Characterization of Ophiolite Lithologies in the Troodos Ophiolite Complex of Cyprus and its potential in prospecting for massive sulphide deposits, Int. journal remote sensing, 1997, Vol.18, no.6, pp1245-1257
23. Gross, G.A. (1995): Mafic Intrusion-hosted Titanium-iron; in Geology of Canadian Mineral Deposit Types, Eckstrand, O.R., Sinclair, W.D. and Thorpe, R.I, (Editors), Geological Survey of Canada, Geology of Canada, Number 8, pages 573-582.
24. Dr. Hurtado, 2004, Image enhancement and Transformation: Band math and Indices, Digital Image processing, Geophysics 5336.
25. http://speclab.cr.usgs.gov/spectral.lib04/DESCRIPT/hydroxylapatite.ws425.html
26. http://www.science.aster.ersdac.or.jp/en/about_aster/sensor/tokutyou.html
27. ILWIS 3.2.1 Academic help
28. International Fertilizer Development Centre (IFDC), 1987, characterization of a phosphate ore sample from Ethiopia, pp9

29. Inzana, J., Kusky, T.M., Higgs, G., and Tucker, R., 2003**,** Using supervised classifications of Landsat TM band ratio images and Landsat TM band ratio image with radar for geological interpretations of central Madagascar
30. Lucas L.F. Janssen and Gerrit C., Huurneman ,2001), Principle of Remote Sensing, by ITC, Enschede, The Netherlands
31. John A. Richards, 1993, Remote Sensing Digital, An introduction Image Analysis,
32. Floyd F. Sabins, 1986, Remote Sensing Principles and Interpretation, second edition
33. Hunt and Salisbury, 1970, Visible and infrared spectra of minerals and rocks. 1 silicate minerals, Modern Geology, Vol. 4, pp283-300
34. Hunt and Salisbury, 1973, Visible and infrared spectra of minerals and rocks. 6 additional silicates. Modern Geology, Vol. 4, pp. 85-106.
35. E. Saroglu, et al., ( ), Fusion of Multi-sensor Remote sensing Data: Assessing the quality of resulting image
36. Shafer, G., 1976, A Mathematical Theory of Evidence Princeton university press, Princeton, N.J., 297pp.
37. Sisay A., 1992, Apatite and Magnetite- Ilmenite resources of the Bikilal Layered Gabbro Complex, pp26
38. Spectral International Inc., (SII), PIMA application, http://www.pimausa.com/pima2.html and PIMA field guide,
39. Wright, D.F. and Bonham-Carter, G.F., 1996, VHMS favorability mapping with GIS-based integration models, Chisel Lake - Anderson Lake area, in Bonham-Carter, G.F., Galley, A.G., and Hall, G.E.M., eds., EXTECH I: A Multidisciplinary Approach to Massive Sulphide Research in the Rusty Lake – Snow Lake Greenstone Belts, Manitoba, Geological Survey of Canada Bulletin 426: Geological Survey of Canada, Ottawa, p. 339-376, 387-401.